



AFRL-OSR-VA-TR-2015-0146

---

## Bonding Unidirectional Carbon Nanotube with Carbon for High Performance

**Yuntian Zhu**  
**North Carolina State University at Raleigh**

---

**06/24/2015**  
**Final Report**

DISTRIBUTION A: Distribution approved for public release.

Air Force Research Laboratory  
AF Office Of Scientific Research (AFOSR)/ RTD  
Arlington, Virginia 22203  
Air Force Materiel Command

REPORT DOCUMENTATION PAGE					Form Approved OMB No. 0704-0188	
<p>The public reporting burden for this collection of information is estimated to average 1 hour per response, including the time for reviewing instructions, searching existing data sources, gathering and maintaining the data needed, and completing and reviewing the collection of information. Send comments regarding this burden estimate or any other aspect of this collection of information, including suggestions for reducing the burden, to the Department of Defense, Executive Service Directorate (0704-0188). Respondents should be aware that notwithstanding any other provision of law, no person shall be subject to any penalty for failing to comply with a collection of information if it does not display a currently valid OMB control number.</p> <p><b>PLEASE DO NOT RETURN YOUR FORM TO THE ABOVE ORGANIZATION.</b></p>						
1. REPORT DATE (DD-MM-YYYY) 13-06-2015		2. REPORT TYPE Final Performance Report		3. DATES COVERED (From - To) March 2012 -March 2015		
4. TITLE AND SUBTITLE Bonding Unidirectional Carbon Nanotube with Carbon for High Performance, Low Density Composites			5a. CONTRACT NUMBER			
			5b. GRANT NUMBER FA9550-12-1-0088			
			5c. PROGRAM ELEMENT NUMBER			
6. AUTHOR(S) Yuntian T. Zhu and Philip Bradford			5d. PROJECT NUMBER 554859;554896			
			5e. TASK NUMBER			
			5f. WORK UNIT NUMBER			
7. PERFORMING ORGANIZATION NAME(S) AND ADDRESS(ES) North Carolina State University, Raleigh, NC				8. PERFORMING ORGANIZATION REPORT NUMBER (1408) 2012-0496		
9. SPONSORING/MONITORING AGENCY NAME(S) AND ADDRESS(ES) Low Density Materials Air Force Office of Scientific Research 875 N. Randolph Street Suite 325, Room 3112 Arlington, VA 22203				10. SPONSOR/MONITOR'S ACRONYM(S) AFOSR		
				11. SPONSOR/MONITOR'S REPORT NUMBER(S)		
12. DISTRIBUTION/AVAILABILITY STATEMENT Distribution A-Approved for Public Release						
13. SUPPLEMENTARY NOTES						
14. ABSTRACT Producing unidirectional carbon nanotube (CNT) composites with a structural morphology identical to aerospace grade carbon fiber composites is a challenging task that until this work, no research groups had accomplished. This research team demonstrated the ability to produce high volume fraction CNT composites with a high level of alignment, low level of CNT waviness and uniform distribution of polymer surrounding the CNTs. This was accomplished through a process called spray winding. In this process polymer solution was sprayed onto aligned CNT sheets as they were taken up onto a mandrel. In addition, a micro-combing technique was developed where a razor blade was used to further aligned and straighten CNTs within the CNT sheets during winding. The ability to integrate a matrix material at the molecular level among long, highly aligned CNTs allowed for record breaking specific strengths, higher than their carbon fiber composite counterparts. In addition to CNT-polymer matrix composites, the team produced CNT-carbon matrix composites that have a morphology that resembles carbon fiber-carbon composites utilized in the aerospace industry, with a nanostructured architecture of aligned CNTs.						
15. SUBJECT TERMS Carbon nanotube composite; Carbon matrix; Polymer matrix; High strength; CNT foams						
16. SECURITY CLASSIFICATION OF: a. REPORT U			17. LIMITATION OF ABSTRACT b. ABSTRACT U	18. NUMBER OF PAGES c. THIS PAGE U	19a. NAME OF RESPONSIBLE PERSON Yuntian Zhu 19b. TELEPHONE NUMBER (Include area code) 919-513-0559	

## INSTRUCTIONS FOR COMPLETING SF 298

- 1. REPORT DATE.** Full publication date, including day, month, if available. Must cite at least the year and be Year 2000 compliant, e.g. 30-06-1998; xx-06-1998; xx-xx-1998.
- 2. REPORT TYPE.** State the type of report, such as final, technical, interim, memorandum, master's thesis, progress, quarterly, research, special, group study, etc.
- 3. DATES COVERED.** Indicate the time during which the work was performed and the report was written, e.g., Jun 1997 - Jun 1998; 1-10 Jun 1996; May - Nov 1998; Nov 1998.
- 4. TITLE.** Enter title and subtitle with volume number and part number, if applicable. On classified documents, enter the title classification in parentheses.
- 5a. CONTRACT NUMBER.** Enter all contract numbers as they appear in the report, e.g. F33615-86-C-5169.
- 5b. GRANT NUMBER.** Enter all grant numbers as they appear in the report, e.g. AFOSR-82-1234.
- 5c. PROGRAM ELEMENT NUMBER.** Enter all program element numbers as they appear in the report, e.g. 61101A.
- 5d. PROJECT NUMBER.** Enter all project numbers as they appear in the report, e.g. 1F665702D1257; ILIR.
- 5e. TASK NUMBER.** Enter all task numbers as they appear in the report, e.g. 05; RF0330201; T4112.
- 5f. WORK UNIT NUMBER.** Enter all work unit numbers as they appear in the report, e.g. 001; AFAPL30480105.
- 6. AUTHOR(S).** Enter name(s) of person(s) responsible for writing the report, performing the research, or credited with the content of the report. The form of entry is the last name, first name, middle initial, and additional qualifiers separated by commas, e.g. Smith, Richard, J, Jr.
- 7. PERFORMING ORGANIZATION NAME(S) AND ADDRESS(ES).** Self-explanatory.
- 8. PERFORMING ORGANIZATION REPORT NUMBER.** Enter all unique alphanumeric report numbers assigned by the performing organization, e.g. BRL-1234; AFWL-TR-85-4017-Vol-21-PT-2.
- 9. SPONSORING/MONITORING AGENCY NAME(S) AND ADDRESS(ES).** Enter the name and address of the organization(s) financially responsible for and monitoring the work.
- 10. SPONSOR/MONITOR'S ACRONYM(S).** Enter, if available, e.g. BRL, ARDEC, NADC.
- 11. SPONSOR/MONITOR'S REPORT NUMBER(S).** Enter report number as assigned by the sponsoring/monitoring agency, if available, e.g. BRL-TR-829; -215.
- 12. DISTRIBUTION/AVAILABILITY STATEMENT.** Use agency-mandated availability statements to indicate the public availability or distribution limitations of the report. If additional limitations/ restrictions or special markings are indicated, follow agency authorization procedures, e.g. RD/FRD, PROPIN, ITAR, etc. Include copyright information.
- 13. SUPPLEMENTARY NOTES.** Enter information not included elsewhere such as: prepared in cooperation with; translation of; report supersedes; old edition number, etc.
- 14. ABSTRACT.** A brief (approximately 200 words) factual summary of the most significant information.
- 15. SUBJECT TERMS.** Key words or phrases identifying major concepts in the report.
- 16. SECURITY CLASSIFICATION.** Enter security classification in accordance with security classification regulations, e.g. U, C, S, etc. If this form contains classified information, stamp classification level on the top and bottom of this page.
- 17. LIMITATION OF ABSTRACT.** This block must be completed to assign a distribution limitation to the abstract. Enter UU (Unclassified Unlimited) or SAR (Same as Report). An entry in this block is necessary if the abstract is to be limited.

## **Final Report**

### **Bonding Unidirectional Carbon Nanotube with Carbon for High Performance, Low Density Composites**

Grant #: FA9550-12-1-0088

Funding period: 3/15/2012-3/15/2015

**Low Density Materials Program**

**Air Force Office of Scientific Research**

Principle Investigators

Yuntian Zhu and Philip Bradford

Department of Materials Science and Engineering

North Carolina State University

Raleigh, NC 27695-7919

## **Abstract**

Producing unidirectional carbon nanotube (CNT) composites with a structural morphology identical to aerospace grade carbon fiber composites is a challenging task that until this work, no research groups had accomplished. This research team demonstrated the ability to produce high volume fraction CNT composites with a high level of alignment, low level of CNT waviness and uniform distribution of polymer surrounding the CNTs. This was accomplished through a process called spray winding. In this process polymer solution was sprayed onto aligned CNT sheets as they were taken up onto a mandrel. In addition, a micro-combing technique was developed where a razor blade was used to further align and straighten CNTs within the CNT sheets during winding. The ability to integrate a matrix material at the molecular level among long, highly aligned CNTs allowed for record breaking specific strengths, higher than their carbon fiber composite counterparts. In addition to CNT-polymer matrix composites, the team produced CNT-carbon matrix composites that have a morphology that resembles carbon fiber-carbon composites utilized in the aerospace industry, with a nanostructured architecture of aligned CNTs.

## **Objectives of this project**

The objective of this project is to produce ultrastrong, low-density carbon nanotube (CNT) composites with record-breaking strengths that are superior to conventional carbon fiber composite. The CNT composites will resemble carbon-carbon and carbon-polymer composites utilized in the aerospace industry with a nanostructured architecture of high volume fraction of aligned long carbon nanotubes.

## **Major accomplishments**

Multiple separate but related studies were conducted throughout the course of the performance period. The most important of these studies (which formed the basis for peer reviewed papers accepted during this project) are covered in the six major sections that follow.

### **1. Aligned Carbon Nanotube/Carbon Matrix Composites**

In this work, we fabricated CNT/polyacrylonitrile (PAN) precursor composites with high degree of CNT alignment, and carbonized and graphitized them at high temperatures. Carbonizing the precursor composites significantly improved their elastic modulus, strength, and electrical conductivity. The matrix was uniformly carbonized and highly graphitized. The excellent mechanical and electrical properties make the CNT/C composites promising for many high temperature aerospace applications.

## 1.1 Experimental

### 1.1.1 Precursor Composites Fabrication

CNT/PAN precursor composites were fabricated using one-step winding infiltration approach. CNT arrays were synthesized from one step chemical vapor deposition (CVD) method using  $\text{FeCl}_2$  as catalyst. The CNTs were multi-walled (MWNTs) with outer diameter of 25-60 nm, as shown in Figure 1.1, and had a length of 1 mm. PAN with an average molecular weight of 150,000 obtained from Sigma–Aldrich, was used as the matrix precursor. Dimethylformamide (DMF) (99.8%, Sigma–Aldrich) was used as the solvent. CNT/PAN films with different CNT weight fractions were fabricated by using PAN/DMF solutions of different concentrations, specifically 10, 20 and 50 g/L. Unidirectional CNT sheets were drawn from spinnable CNT arrays and wound onto a rotating Polytetrafluoroethylene (PTFE) spool. During the CNT sheet winding, PAN/DMF solution droplets were applied layer by layer on the sheets to ensure sufficient infiltration. The films were then vacuum dried to remove any residual solvent and then hot-pressed at 160 °C for 2h. The resultant samples had a thickness of 10~20  $\mu\text{m}$  and were cut into strips with dimensions of 15×0.5 mm.

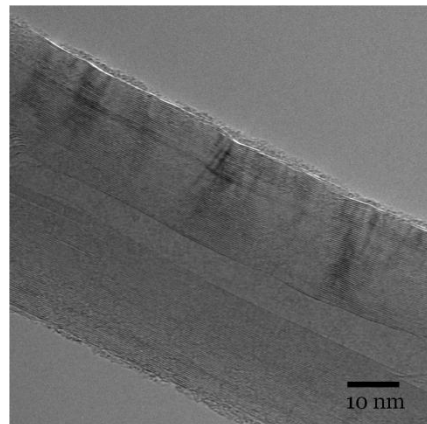


**Figure 1.1** TEM image of an individual CNT

### 1.1.2 Stabilization and Pyrolysis Process

The precursor films were first heat-treated in air to stabilize and oxidize the PAN matrix. A tension device was used to keep the films under tension during the heat treatment. The samples were heated to 250 °C at a heating rate of 5 °C/min and then held for 120 min, followed by heating up to 320 °C at a heating rate of 1 °C/min and then held for 25 min.

The stabilized samples were carbonized at 1300 °C in a vacuum furnace for 60 min under vacuum (below 1E-2 milibar) after an initial ramping at 5 °C/min. A set of the samples was then heated in argon gas (99.999% and then run through an in-line  $\text{O}_2/\text{H}_2\text{O}$  trap) to graphitize them. They were first heated up to 1500 °C at 25 °C/min and held for 15 min, then heated to 2000 °C at 15 °C/min and held for 15 min. Finally, the treatment temperature ramped to 2150 °C at 3 °C/min and held for 30 min. The films were sandwiched and pressed between two polished graphite plates during carbonization and graphitization.

### 1.1.3 Materials Characterizations and Testing

Scanning electron microscopy (SEM) analysis of the CNTs network and composite fracture surface was carried out on a JEOL 6400F microscope at an acceleration voltage of 5kV. Raman spectra were recorded with a Renishaw Ramascope. The laser has a wavelength of 632 nm and a spot size of about 1~2  $\mu\text{m}$ .

Mechanical property testing was performed using a Shimadzu EZ-S tensile testing machine at a crosshead speed of 0.5 mm/min and a gauge length of 10 mm. The sample thickness was measured with a micrometer and verified by SEM image. At least five samples were tested for each composite group. Electrical resistance was measured using the two-probe method by a 34410A 6.5 digit multimeter. Silver epoxy obtained from SRA Soldering Products was coated on the sample as an electrode.

## 1.2 Results and Discussion

### 1.2.1 Mechanical Properties

The mechanical properties of precursor and carbonized composites are summarized in Table 1.1 Figure 1.2 shows the typical stress-strain curves of composite films made using the 10 and 20 g/L PAN solutions, respectively. The strength and stiffness increased after carbonization and the tensile failure strain decreased. When using the 20 g/L concentration, the carbonized composites showed stiffness up to 143 GPa and strength up to 551 MPa, which were 200% and 58% improvement, respectively, comparing to their precursor composites. The carbonized composites obtained at both 10 and 50 g/L concentrations have lower property values, which suggests that 20 g/L may be close to the optimal concentration.

It should be noted that in the current work, CNT functionalization was purposefully avoided due to the potential damages to CNTs and the uncertainty on their effect on carbonization. Millimeter-long CNTs were used to develop effective load transfer over their length through van der Waals interactions with the matrix. In addition, high temperature has been shown to induce graphitic structure formation from PAN in the interphase region, which can improve the interaction between CNTs and the matrix. The formation of this structure is expected to enhance the mechanical properties of the composites. The carbon matrix is more brittle than the PAN matrix making the CNT/C composites more sensitive to flaws, giving a lower failure strain in comparison to the CNT/PAN composites.

**Table 1.1** Mechanical properties of precursor and carbonized composite films

PAN solution Concentration (g/L)	Composite Sample	Young's Modulus (GPa)	% Increase	Tensile Strength (MPa)	Strain (%)
10	Precursor	$30.0 \pm 8.8$	112%	$287.5 \pm 93.4$	$0.85 \pm 0.23$
	Carbonized	$63.6 \pm 18.6$		$317.5 \pm 94.1$	$0.56 \pm 0.15$

20	Precursor	$31.7 \pm 9.8$	200%	$292.0 \pm 51.6$	$1.03 \pm 0.42$
	Carbonized	$95.2 \pm 26.5$		$460.2 \pm 96.2$	$0.53 \pm 0.22$
50	Precursor	$16.2 \pm 4.2$	201%	$109.8 \pm 36.6$	$0.80 \pm 0.20$
	Carbonized	$48.8 \pm 7.2$		$170.0 \pm 26.5$	$0.61 \pm 0.08$

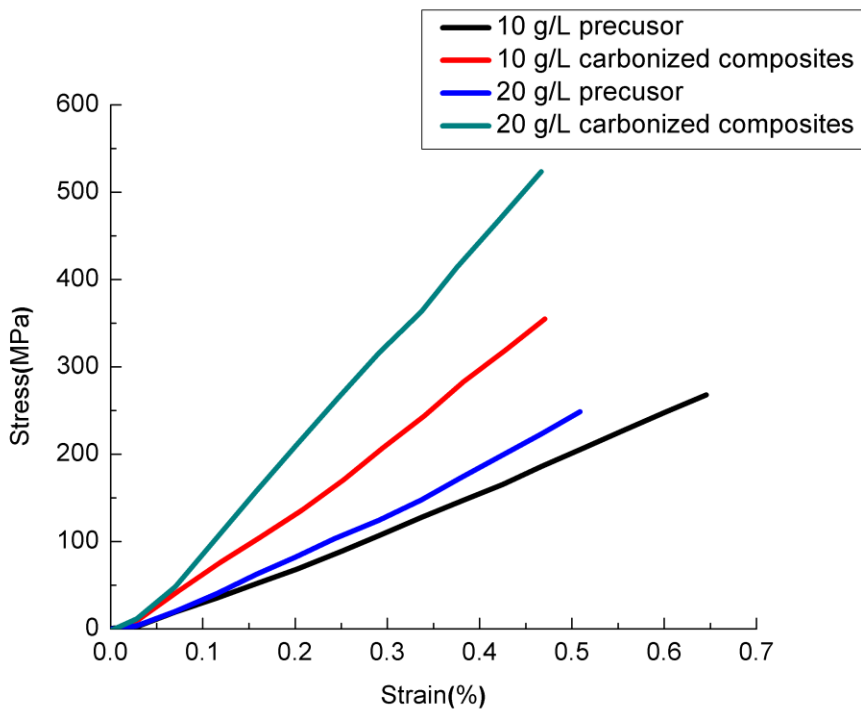


**Figure 1.2** Typical stress-strain curves of precursor and carbonized composite films.

In real-world aerospace applications, a stronger and lighter material is critical in terms of saving energy and enabling advanced technologies. Typical C/C composites have a density of  $1.6\text{--}2.0 \text{ g/cm}^3$ . The aligned CNT/C composites presented in this study have a density of  $1.1 \text{ g/cm}^3$ . Consequently, their specific strength is comparable to some of the best C/C composite properties presented in the literature. The tensile strengths of previously reported CNT/C composites are far lower. The comparison is shown in Figure 1.3.

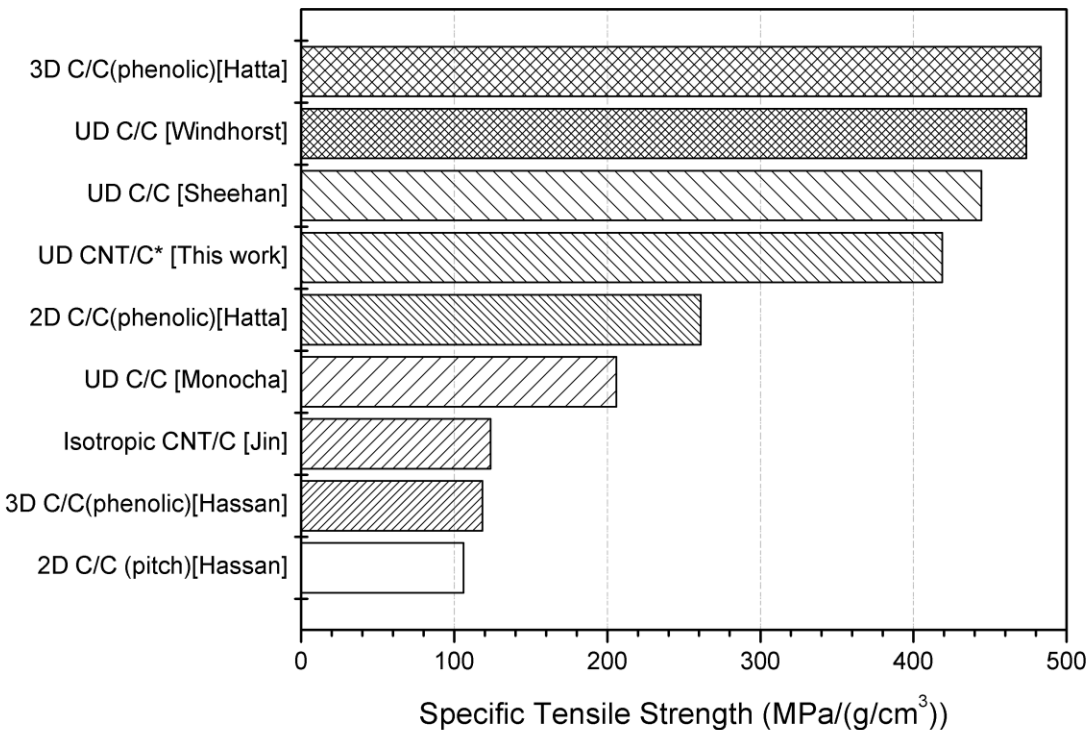


**Figure 1.3** Comparison of the specific tensile strength with C/C composites and other reported CNT/C composites. UD means unidirectional.

## 1.2.2 Electrical Properties

The electrical conductivity of C/C composites is an important property needed for some applications in aerospace composites. Although CNTs have excellent electrical conductivity, the incorporation of insulating polymer surrounding the CNTs in the composites leads to a relatively high resistance. Table 1.2 shows the electrical properties of the CNT/PAN precursor composites and CNT/C composite films. The carbon matrix has a much higher electrical conductivity than PAN polymer, giving rise to a much higher electrical conductivity of the CNT/C composites. It was observed that the electrical conductivity of the composites (both CNT/PAN and CNT/C) increased with decreasing concentration of the PAN solution. The lower solution concentrations left less polymer between CNTs after evaporation, increasing the CNT fiber volume fraction. When graphitization of the CNT/PAN composite was performed the electrical conductivity was increased by one order of magnitude, from 39 to 392 S/cm, which can be attributed to the increased graphitization degree of carbon.

**Table 1.2** Electrical properties of precursor and CNT/C composite films

PAN Concentration (g/L)	Sample	Electrical Resistivity ( $\Omega \cdot \text{cm}$ )	Electrical Conductivity (S/cm)	% Increase
10	Precursor	$1.1 \times 10^{-2}$	94	289%
	Carbonized	$2.7 \times 10^{-3}$	368	
20	Precursor	$3.1 \times 10^{-2}$	39	385%
	Carbonized	$8.7 \times 10^{-3}$	190	
	Graphitized	$2.6 \times 10^{-3}$	392	919%
50	Precursor	$6.5 \times 10^{-2}$	16	622%
	Carbonized	$8.6 \times 10^{-3}$	117	

## **2. Structural Annealing of Carbon Coated Aligned Multi-Walled Carbon Nanotube Sheets**

Sheets of aligned multi-walled carbon nanotubes (AMWCNTs) were used to study the structural annealing of pyrolytic carbon (PyC) coatings with various thicknesses on MWCNTs. PyC was deposited using chemical vapor infiltration and the thickness was controlled via the infiltration time. Structural annealing of the PyC coated AMWCNT (AMWCNT/C) sheets at 2150 °C provided different results for different thickness coatings. Transmission electron microscopy images showed that the carbon deposited from acetylene formed laminar PyC coatings, resembling rough tube walls, on the CNT surfaces. Following the high temperature heat treatment, coatings from short PyC deposition times changed their structure, resulting in radial growth of the MWCNTs. Raman and X-ray diffraction measurements also revealed that the radially grown MWCNTs had graphitic quality very close to pristine nanotubes after annealing. Electrical conductivity of AMWCNT/C sheets after high temperature heat treatment was twice that of pristine AMWCNT sheets. The focus of this study was to determine the PyC coating thickness at which a rough PyC coating would no longer change its structure into new CNT walls. The samples treated longer than 30 minutes had much more disordered PyC deposited on the surface and the additional material did not form additional tube walls after thermal annealing.

### **2.1 Experimental**

#### **2.1.1 Synthesis of MWCNTs**

Vertically aligned CNT arrays were fabricated using a modified version of the chlorine mediated chemical vapor deposition route. The arrays were grown on a quartz substrate in a tube furnace at 760 °C with acetylene as the carbon precursor and  $\text{FeCl}_2$  (anhydrous 99.5% VWR) as the catalyst. The process gases consisted of acetylene (600 sccm), argon (395 sccm) and chlorine (5 sccm). Growth pressure was maintained at 3 Torr. After 15 minutes of growth, the system was allowed to cool to room temperature while purging with argon. The resulting arrays were ~ 2

mm tall containing MWCNTs with an average diameter  $\sim 29\pm8$  nm. The as-grown arrays were easily drawn into AMWCNT sheets.

After cleaning the furnace tube, the as-grown arrays were reloaded inside the tube furnace and underwent a chlorine treatment at 760 °C for 15 minutes while the pressure of the system was maintained at 3 Torr. Iron quickly reacts with chlorine at high temperatures to produce  $\text{FeCl}_2$  which then vaporizes and leaves the process tube. After the chlorine treatment, energy dispersive X-ray spectroscopy showed that the iron level decreased from 1.5 to 0.53 wt%. Any iron remaining after the chlorine treatment was thought to reside inside of the CNTs. For this study it was important to remove as much iron as possible to avoid possible secondary reactions, to ensure that it would not influence the final morphology of the heat treated carbon structures.

### 2.1.2 AMWCNT/C Composite Fabrication

The concept of dry, continuous drawing of CNTs for fabrication of yarns and AMWCNT sheets is now quite common. This technique was used to produce the AMWCNT/C structures in this work. To minimize potential variability that naturally comes from batch CNT growth, all of the samples utilized in this study were produced from arrays from a single growth run. Figure 2.1 shows a schematic of the processing of the AMWCNT/C sheets. First, single layer AMWCNT sheets were wrapped around multiple graphite frames for further processing. Single layer AMWCNT sheets were used in the first set of experiments to ensure maximum carbon deposition uniformity. The single sheets had a thickness of approximately 20  $\mu\text{m}$  with a very low density ( $0.002 \text{ g/cm}^3$ ). This significantly reduced the potential of PyC coating variation due to diffusion length of the carbon source gases. In the next step, the AMWCNT wrapped graphite frames were placed inside the tube furnace and PyC was deposited on them using CVI, with acetylene as carbon source. Samples were heated in vacuum and once the temperature reached 800 °C, acetylene was released into the system at a flow rate of 600 sccm while pressure was maintained at 30 Torr for the desired deposition time (0, 10, 20, 30, 40 or 80 minutes). These samples are referred to as pristine, 10-C, 20-C, 30-C, 40-C and 80-C, respectively.

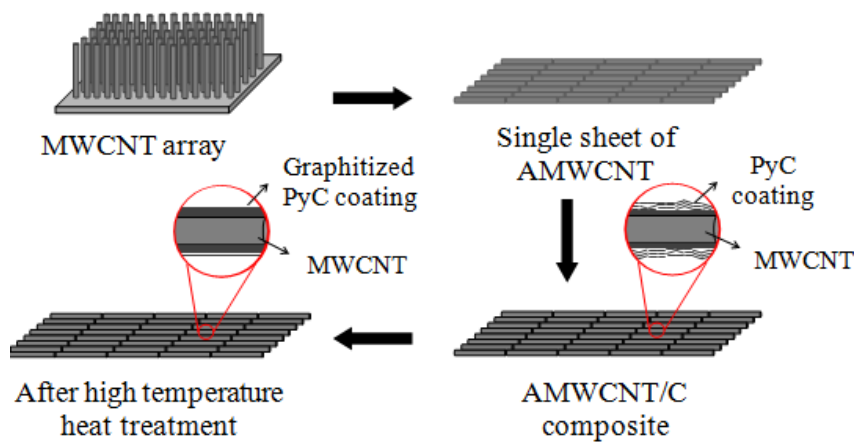


**Figure 2.1** Schematic of a single sheet AMWCNT/C composite going through the multiple processing steps.

A portion of the PyC coated AMWCNT sheet was removed from each sample for analysis. The remaining portions of the samples were further heat treated in a high temperature furnace (RED DEVIL vacuum furnace WEBB 124) at 2150 °C (maximum furnace temperature) for five hours in an argon atmosphere. The supplied argon had an initial purity of 99.999%. An in-line Concoa 580-1600 series oxygen/H<sub>2</sub>O trap was also used to further reduce the concentration of oxidizing gases. This trap is capable of reducing the oxygen content in a gas stream to less than 15 ppb. The heat treated samples were labeled and referred to as pristine-G, 10-G, 20-G, 30-G, 40-G and 80-G after heat treatment. Figure 2.2 shows the steps taken to make the AMWCNT/C sheets.

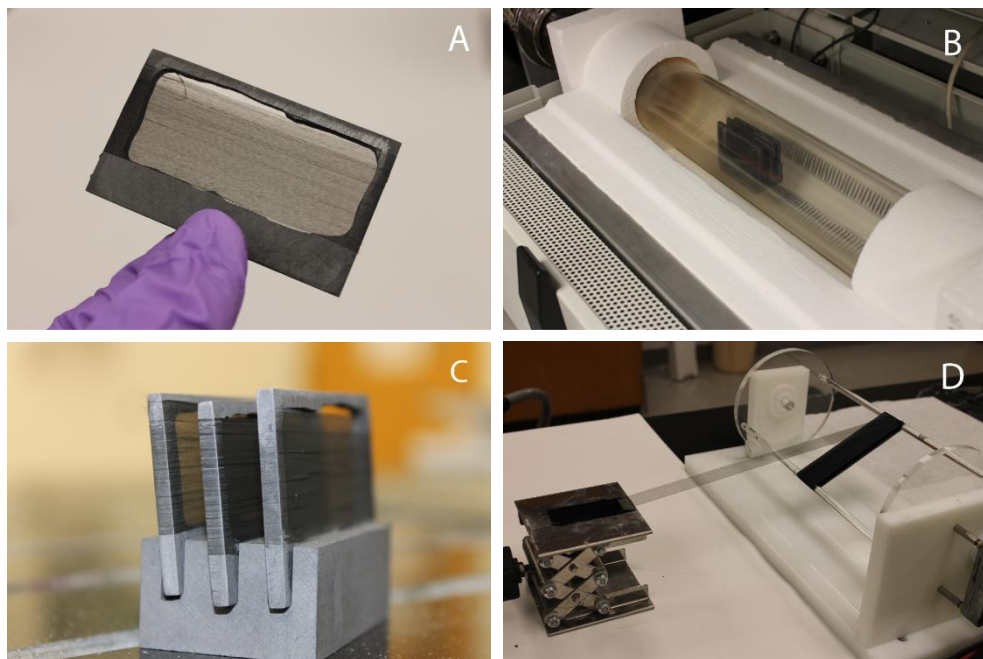


**Figure 2.2** Procedure for AMWCNT/C composite sheet fabrication. A) A single sheet of AMWCNT wrapped around a graphite frame. B) AMWCNT wrapped graphite frames placed vertically onto a crucible holder inside the furnace for CVI of PyC. C) Single sheets of AMWCNT/C after PyC deposition. D) Dry drawing of thicker, multi-layer AMWCNT sheets.

These single sheet AMWCNT/C structures were used for Transmission Electron Microscopy (TEM) and Raman studies. Thicker samples were needed for X-ray diffraction (XRD), Thermogravimetric analysis (TGA) and electrical property analysis to increase accuracy of the measurements. To make thicker structures, the AMWCNT sheets were drawn from the array and continuously collected around two parallel glass rods rotating at 13 rpm. After 8 minutes of winding, the resulting multi-layer AMWCNT sheet was ~ 3 mm thick. These thick sheets were then separated from the glass rods using a razor and were placed inside the CVI furnace for PyC coating of 0, 30 or 80 minutes. This was followed by high temperature heat treatment of the samples. The conditions for PyC coating and heat treatment were the same as for the single layer AMWCNT/C sheets.

### 2.1.3 Characterization

Density values were calculated using the physical dimensions of the samples obtained by a calibrated scale bar in a stereo microscope, and the mass of the samples measured with an analytical balance with readability to 0.1 mg. After calculating the density of the pristine samples, they were PyC treated and the density was recalculated. The same samples were then heat treated and the density was recalculated again. Using the same samples throughout each step of the process allowed us to compare densities after each step without having a large number of samples.

TEM images were obtained using a JEOL 2000FX TEM operating at 200 kV. The TEM samples were prepared by dispersing a small amount of the AMWCNT/C sheet in chloroform using sonication. Following sonication, a droplet of the dispersion was deposited on a carbon mesh TEM grid and allowed to dry. To calculate the average diameter and diameter distribution, 100 measurements were taken from TEM images for each sample using ImageJ software. A Renishaw 2000 Raman microscope with a laser wavelength of 514 nm (50x magnification) was used to analyze the quality of each structure. The single layer AMWCNT/C sheets were mounted to a microscope slide prior to spectrum acquisition and at least five spectra were obtained in different locations across each sample.

Diffraction experiments were performed on a PANalytical Empyrean diffractometer with a 7-circle goniometer configuration, using a Cu K $\alpha$  source with a wavelength,  $\lambda = 1.5406 \text{ \AA}$ . A continuous, coupled scan ( $2\theta-\omega$ ) was taken for each sample for  $2\theta = 20-60^\circ$ . As mentioned earlier, thicker samples were fabricated for X-ray, TGA and electrical property measurements. However, due to the low density of thick sheets and the interaction depth limitation, the signal strength for X-ray measurements was lower than expected. To increase signal intensity, samples were compressed and densified by infiltrating dilute epoxy solution and further curing the composite under pressure. A piece of quartz filter paper was placed under the composite before curing to absorb excess resin solution. The background for the amorphous epoxy and quartz was measured and subtracted from the final spectra for each sample. Samples were placed so that nanotubes were aligned parallel to the sample stage.

TGA experiments were conducted on a Perkin Elmer Pyris 1 TGA, where 5-10 mg of each sample was heated at a rate of 20  $^\circ\text{C}/\text{min}$  in air to 900  $^\circ\text{C}$ . Electrical properties of the AMWCNT/C sheets were measured using a four probe resistance measurement system. The samples were placed onto a glass plate across four parallel gold line electrodes. A square shaped piece of glass along with a 500 g weight was placed on top of the sample to ensure consistent contact between sample and all four gold electrodes during resistance measurements.

## 2.2 Results and Discussion

Raman spectroscopy was used to compare the structure of arrays before and after the chlorine treatment. Generally, the G peak (centered around  $1580 \text{ cm}^{-1}$  in SWNT) originates from the perfect graphite crystal structure while D peak (centered around  $1350 \text{ cm}^{-1}$  in SWNT) originates from the defects in the structure. The integrated intensity ratio of disordered to graphitic carbon ( $R = I_D/I_G$ ) was used to evaluate the defect density of carbon materials. After the chlorine treatment, the average R changed from 0.45 to 0.41 indicating a slight improvement in the quality of the MWCNT arrays. Raman spectra of the arrays collected before and after chlorine treatment are provided in the supporting information.

Table 2.1 shows the variation in average CNT diameter with PyC deposition time. CNT diameter increased significantly with increasing CVI time. The thickness of the PyC layer (half of the difference between diameter of PyC coated CNTs and pristine CNT diameter) increased from 3 nm after 10 minute PyC deposition to 34 nm after 80 minute PyC deposition. The diameter distribution of coated CNTs also broadened as deposition time increased. The use of a single layer CNT sheet ruled out the possibility of deposition variation due to a diffusion length limitation. The reason for a larger diameter distribution for longer PyC coating times is not understood at this time.

**Table 2.1** Average CNT diameter for different PyC deposition times

Infiltration (min)	Time	Avg CNT diameter (nm)
0		29±8
10		35±7
20		37±7
30		44±10
40		50±12
80		97±16

Figure 2.3 shows density variation with different PyC coating times, before and after high temperature heat treatment. Pristine sheets of AMWCNTs (0 minute carbon treatment time) are very low density structures with apparent density of ~ 0.002 g/cm<sup>3</sup>. After 30 and 80 minutes of PyC deposition, apparent density increased to 0.004 and 0.007 g/cm<sup>3</sup> respectively. Density of the structures did not change significantly after high temperature heat treatment. The outer dimensions of the multi-layer AMWCNT sheet samples did not change after PyC deposition or heat treatment. While the mass (and therefore density) of the PyC coated structures increased fairly linearly with coating time, the change in tube diameter did not. The much larger tube diameters at the longest deposition time were attributed to the decreasing level of structural order and corresponding decreased local density of the outermost PyC layers.

While the CNT diameters were increased significantly, it is unlikely that this increase (and subsequent narrowing of the space between the CNTs) had an effect on the deposition mechanism of the PyC as the deposition time increased. Even the AMWCNT/C sheet samples treated for the longest time of 80 minutes had an aerogel-like density, with CNT packing density lower than even the as-grown CNT array. This highly porous nature, where inter-tube spacing is hundreds of nanometers, is conducive for gas diffusion through the structure at the deposition pressure utilized in this study.

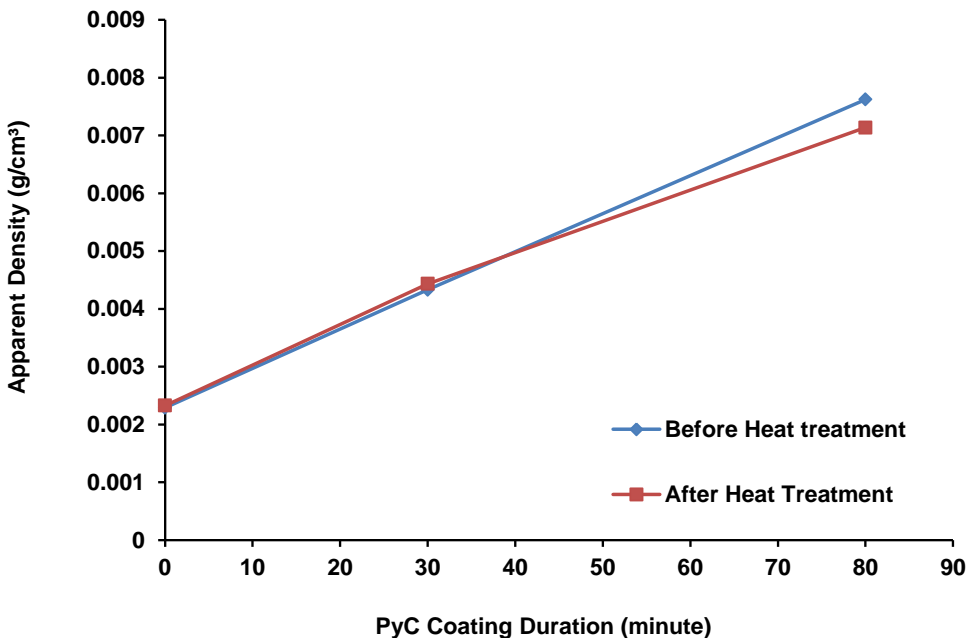


**Figure 2.3** Changes in the density of thick multi-layered AMWCNT/C sheets with different PyC coating durations.

### 2.2.1 Morphology of AMWCNT/C composites

TEM images in Figures 2.4 and 2.5 show the structures of samples coated for 10, 20, 30, 40 and 80 minutes before and after heat treatment. Generally, the deposited PyC exhibited two morphologies, transitioning from rough laminar PyC deposited on the surface of CNTs toward disordered carbon at the outermost surface of the coating. Further comparison between these images in Figures 2.4 and 2.5 shows that by increasing carbon treatment time and thickening the PyC layer, the deposited layers became more disordered and contained more curved carbon segments which resulted in disinclination of parallel carbon layers and thus, the surface of the coating layer became less smooth and less dense. One of the possible reasons for this is further explored in a later section.

The PyC layer was also discontinuous in some areas across the length of CNTs. Another possible reason is that at some points, the MWCNTs within the sheet were touching each other which would suppress PyC deposition in those areas. Those CNTs would then become separated after dispersion.

Images of samples exposed to the heat treatment at 2150° C for five hours showed fewer structural defects in the walls and improved graphitic quality of both the CNT structure and the deposited PyC coating layer. For samples with shorter carbon deposition times (10-G, 20-G and 30-G), the PyC layer rearranged, resulting in a crystalline structure where the coating and original tube walls could not be easily differentiated in the TEM images. In contrast, images of 40-G and 80-G samples showed that while the PyC layers deposited closest to the original

MWCNT developed a structure similar to the CNT walls, carbon layers close to the surface exhibited a more disordered PyC structure, and remained disordered even after the heat treatment.

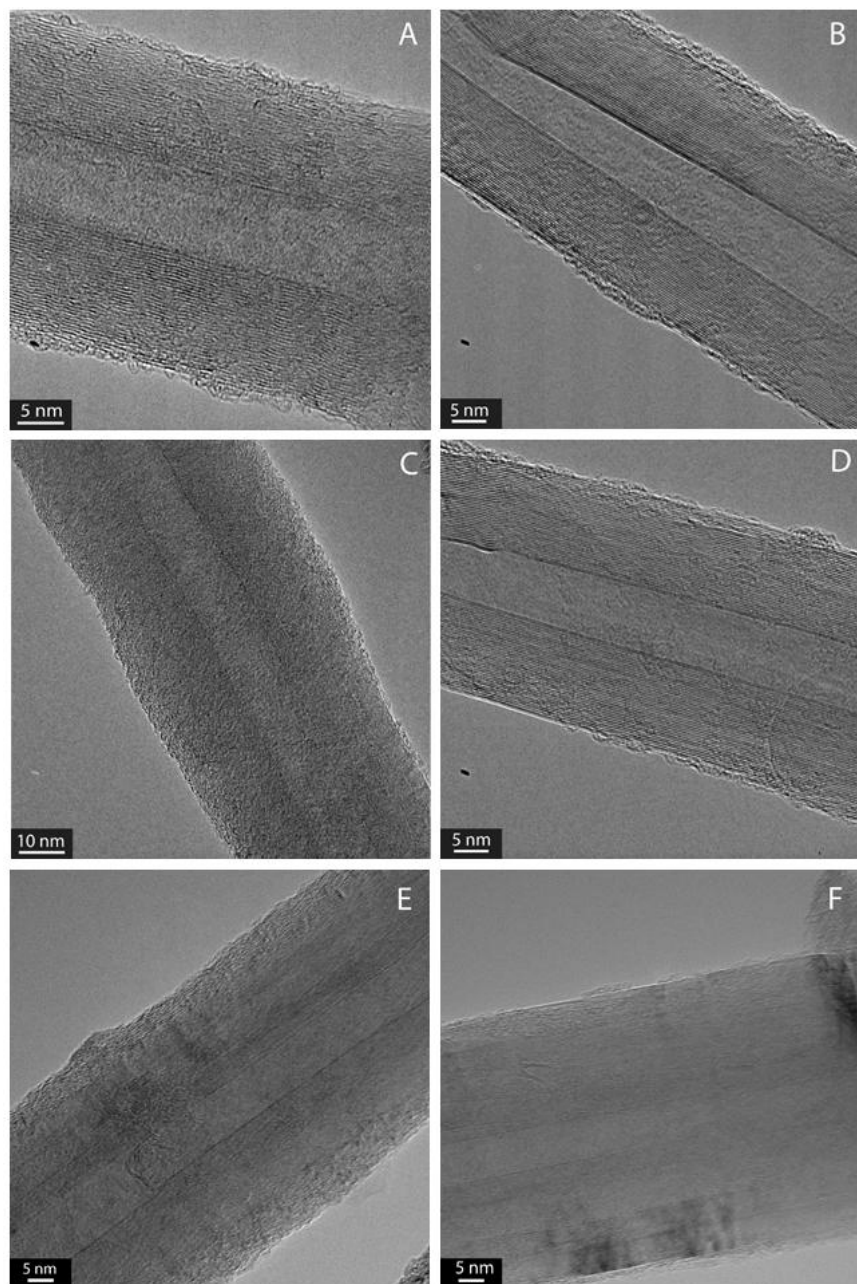


**Figure 2.4** TEM images of PyC coated CNTs before (left column) and after (right column) heat treatment for samples with 10 min (A&B), 20 min (C&D) and 30 min (E&F) PyC coating.

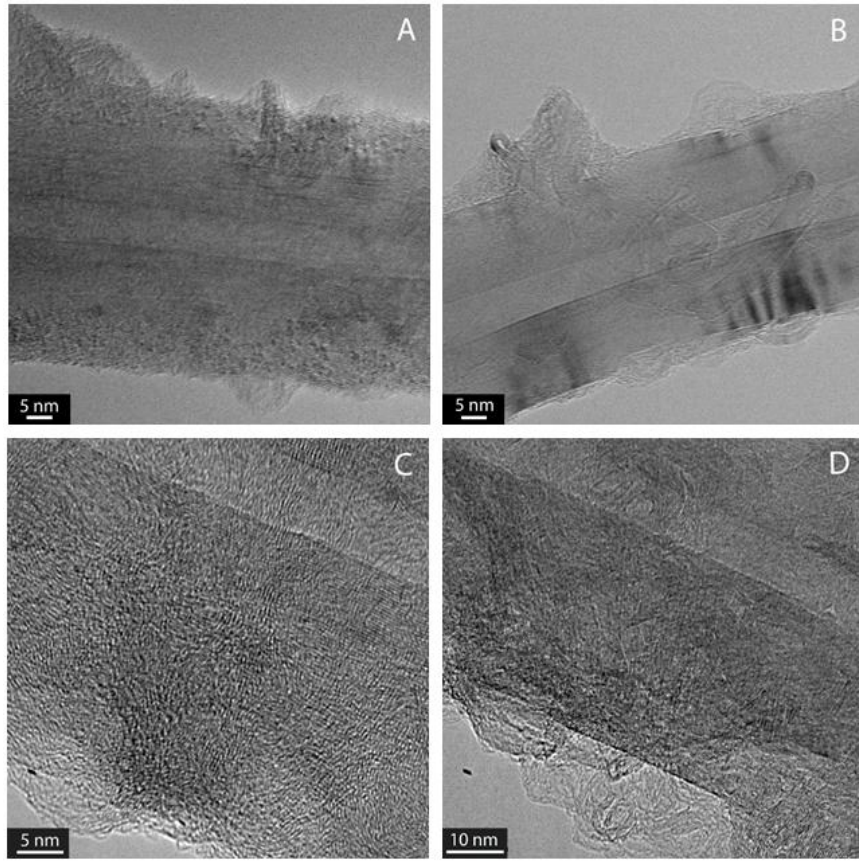


**Figure 2.5** TEM images of PyC coated CNTs before (left column) and after (right column) heat treatment for samples with 40 min (A&B) and 80 min (C&D) PyC coating.

## 2.2.2 Structure of AMWCNT/C sheets

Raman spectroscopy was used to analyze the graphitic structure of pristine and AMWCNT/C sheets. Of particular interest were the G peak and D peak, as they contribute to graphitic and disordered carbon structures respectively. Each sample was scanned at 5 different locations and the average R ( $I_D / I_G$ ) was calculated. As shown in Figure 2.6, increasing the PyC infiltration time increased the average value of R from 0.36 for pristine AMWCNT sheet to 2.12 after 80 minutes PyC infiltration. This indicates that thickening the AMWCNTs with PyC increases the structural disorder. After heat treatment at 2150 °C, the average R for AMWCNT sheets with 10, 20 and 30 minute PyC deposition all decreased to ~ 0.2. This average R ratio was very close to that of the pristine AMWCNT sheet after the same high temperature heat treatment (~ 0.17). While the average R ratios of samples with longer PyC infiltration times ( $\geq 40$  min) also decreased after heat treatment, they yielded higher ratios compared to PyC coated samples treated for shorter times. In addition to the decrease in R ratio, a smaller full width half maximum of both the G band and D band was observed after high temperature heat treatment of the samples. Raman spectra of pristine and PyC coated AMWCNT sheets before and after annealing are provided in the supporting information. The Raman results support the results from

TEM observations and show that there is a limit for the thickness of PyC coating that allows for radial growth of graphitic CNT walls after high temperature heat treatment. For the deposition parameters used in this study, this limit was approximately 30 minutes, after which the additional deposited layer did not reorganize to resemble tube walls and radially grow the MWCNT structure. It is important to note that with different deposition conditions, precursors or original CNT characteristics, the structure of the deposited PyC will be different and thus the maximum thickness of PyC that can structurally annealed into new tube walls may be different as well.

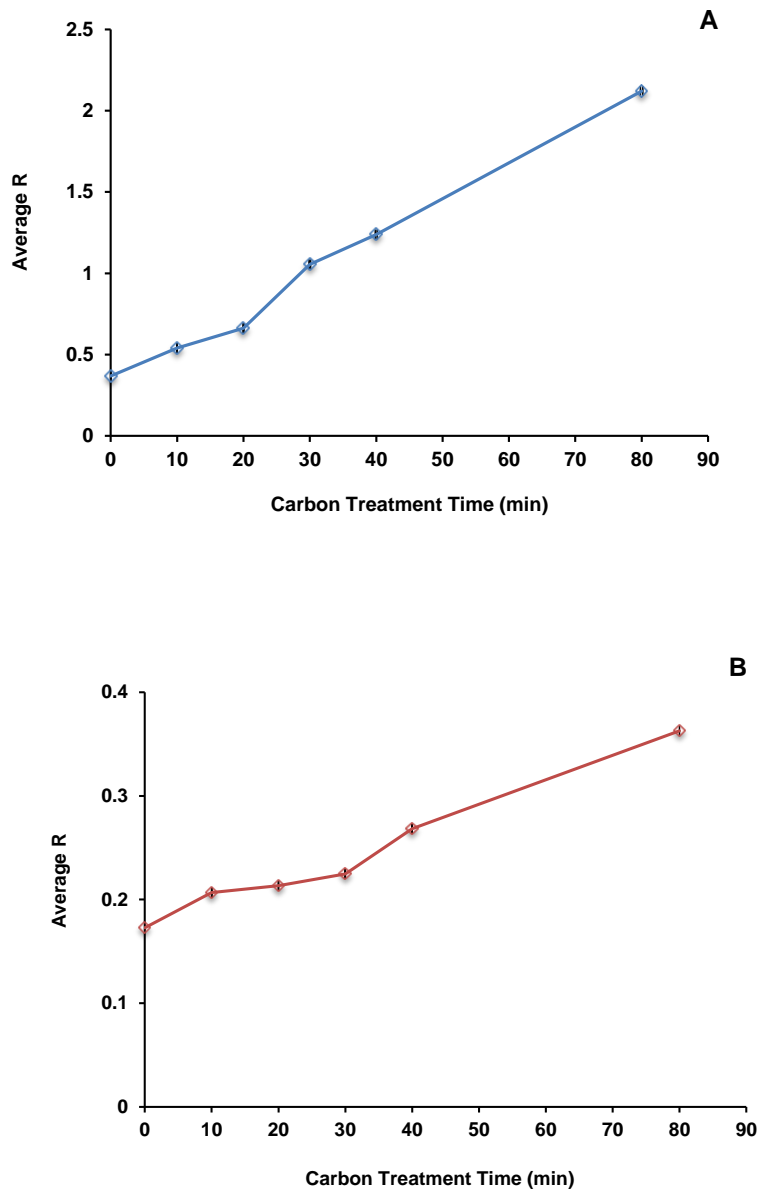


**Figure 2.6** Average R as a function of PyC coating duration before (A) and after heat treatment (B).

XRD spectra of pristine, AMWCNT/C, and heat treated samples are shown in Figure 2.7. Due to the parallel z-axis orientation of the CNTs to the incident beam, the main visible features are the  $00l$  reflections at  $002$  ( $\sim 26^\circ$ ). Based on the position of the  $002$  peak, information about the average interlayer spacing, or d-spacing, can be calculated using the Bragg equation,  $d_{002} = \lambda / 2 \sin \theta_{002}$ . Additionally, the full width half maximum (FWHM) of this peak can be used to calculate the graphite stack size or crystallite size ( $L_c$ ), using Scherrer's equation,  $L_c = \lambda / \beta \cos \theta_{002}$ . In these equations,  $\lambda$  is the x-ray wavelength,  $\theta_{002}$  is the location of the  $002$  reflection, and  $\beta$  is the FWHM of the  $002$  peak. The measured and calculated parameters for each sample are summarized in Table 2.2.

PyC deposited samples have larger d-spacings than pristine CNTs. This indicates that the as-deposited material was rough and poorly graphitized, which is confirmed in the TEM images. The measurable increase in intensity of the  $002$  peak after heat treatment indicates improvement in the interlayer graphitic structure due to removal of defects and carbon atom rearrangement. Significant changes were measured in the stack size of graphite crystallites.  $L_c$  for Pristine was 13.29 nm, and by dividing this number by the characteristic d-spacing, the number of walls,  $n$ , was found to be 39.  $L_c$  increased after annealing sample 30-C due to the radial growth of CNTs and the formation of additional walls, leading to an increase in  $n$  from 39 to 45.  $L_c$  did not continue to increase for sample 80-G however, due to the inability to fully graphitize the deposited PyC during structural annealing. These findings are in agreement with TEM images and Raman results. The decrease in  $L_c$  and  $n$  for 30-C and 80-C&G arises from the disordered structure so that the XRD parameters cannot fully represent the structure of those samples.

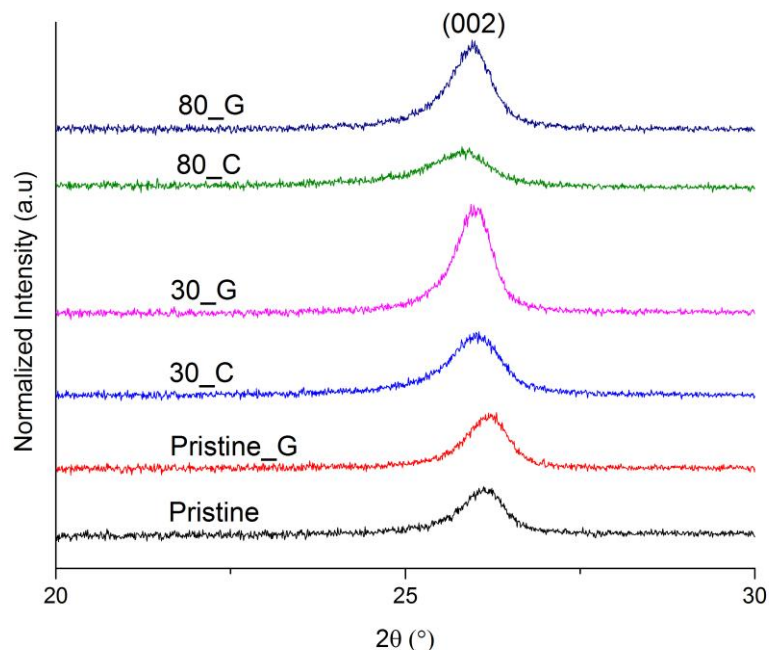


**Figure 2.7** XRD spectra of Pristine, PyC coated and heat treated samples.

**Table 2.2** Measured and calculated structural parameters of the different samples.

Sample	$2\theta$ (degree)	$d_{002}$ (Å)	FWHM (degree)	$L_c$ (nm)	n
Pristine	26.1	3.412	0.7398	13.29	38.95
Pristine_G	26.16	3.403	0.7194	13.67	40.16
30_C	25.99	3.426	0.8855	11.09	32.37
30_G	25.97	3.428	0.6284	15.63	45.58
80_C	25.75	3.458	1.109	8.836	25.55
80_G	25.92	3.434	0.8333	11.78	34.30

Figure 2.8 shows the TGA and derivative TGA curves of the samples. Small mass loss was observed to occur between 200 and 400 °C which was due to the presence of amorphous carbon. The relatively minute amount of mass loss that occurred in this region for all samples (even those deposited with PyC carbon) indicates that they were relatively free of bulk amorphous carbon. The small loss could be attributed to broken or incomplete surface layers of carbon, which would be highly reactive with the oxygen in air. The average onset temperature for AMWCNT sheets prior to heat treatment was 625 °C. After high temperature heat treatment of the samples, the average onset temperature was increased to nearly 750 °C. Annealing healed some of the defects in MWCNTs and PyC coatings, leaving a structure with greater oxidative stability.

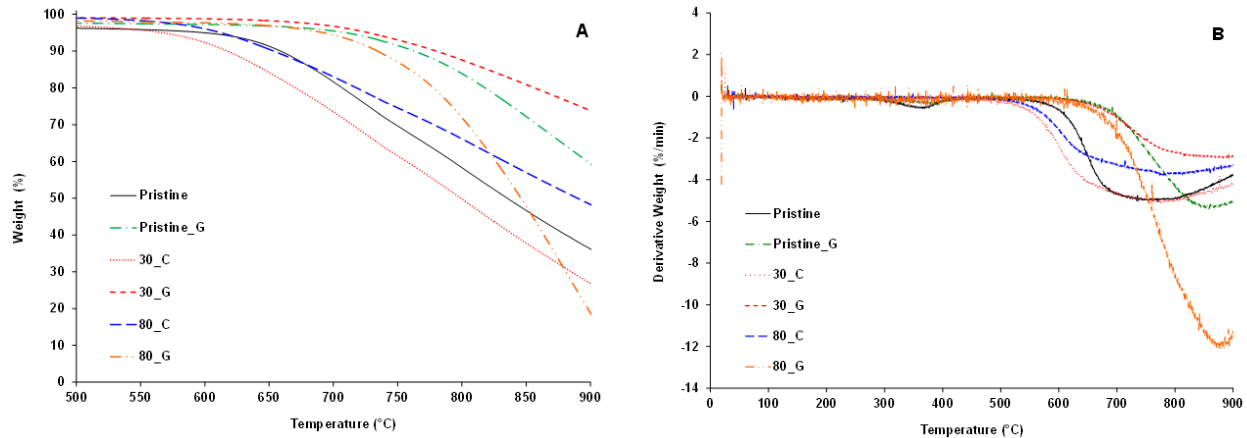


**Figure 2.8** TGA curves (A) and derivative TGA curves (B) of pristine and PyC coated samples.

To support findings from TEM, Raman and XRD analysis, the electrical conductivity of the AMWCNT/C sheets were measured before and after high temperature heat treatment. As shown in Table 2.3, conductivity of pristine AMWCNT sheets increased from 2.03 to 4.1 S/cm after 80 minute PyC treatment with subsequent annealing. This increase was reasonable due to the

addition of electrically conductive material on the original CNT structure of the same physical dimensions. Some of PyC would be deposited at CNT junctions, reducing the contact resistance between CNTs. High temperature heat treatment also improved the conductivity of all of the samples. The results show that the largest increase in conductivity before and after heat treatment was 60%, for the composite with 30 minutes PyC deposition. This supports Raman and XRD data, corresponding well to the structural changes identified in that sample. The 30-G sample had the largest tube diameter and mass increases while still being graphitized well during the high temperature heat treatment. Further PyC deposition increased the mass and diameter of the CNTs, however the inability for the additional layers to graphitize limited the increase in electrical conductivity after heat treatment to 37%.

**Table 2.3** Electrical conductivity of AMWCNT sheets with different PyC coating times.

Sample	Conductivity (S/cm)	Percent Increase
Pristine	2.03	
Pristine-G	2.67	32%
30-C	2.47	
30-G	3.98	60%
80-C	2.98	
80-G	4.10	37%

#### 2.2.4 Effect of MWCNTs quality on the microstructure of PyC coating

Results from TEM observations suggest that the ordered structure of carbon atoms in the initial PyC coating layers was induced by CNTs. Here, to further study the effect of graphitic quality of CNTs on the microstructure of deposited PyC, a single layer sheet of pristine AMWCNT was first annealed at 2150° C for five hours and then coated with PyC for 40 minutes. Figure 2.9 shows a TEM image of this sample (labeled G-40-C). A comparison between this image and Figure 2.5a (for sample 40-C) shows that despite having the same infiltration time of 40 minutes, the PyC coating in G-40-C is more ordered and the outermost surface is smoother. The CNTs with higher quality graphitic walls induced the ordered structure in PyC coating layer over a longer range, which may allow for a further increase in the thickness of PyC that can be recrystallized on the surface of the CNTs. These results also help to explain why the PyC coating on the as-grown CNTs transitions from a rough laminar carbon to disordered carbon as the coating thickness increases. It appears that the quality of the PyC deposited during this process depends of the surface quality of the underlying tube structure (pristine tube or one that has PyC deposited on it). Future work may include a more detailed study in this area.

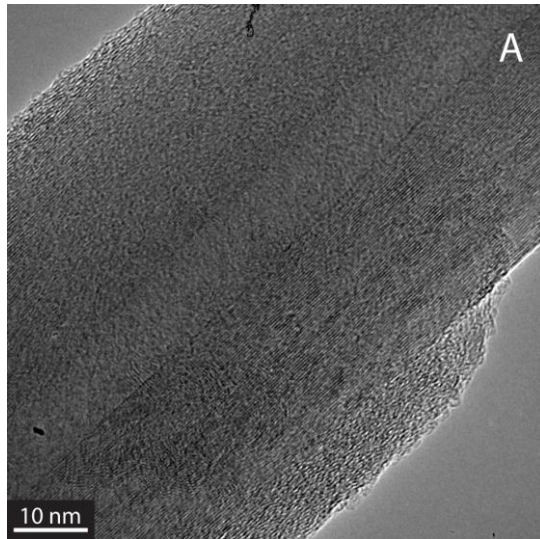


**Figure 2.9** TEM images of 40 min PyC coating on a graphitized pristine CNT.

### **3. Resilient Anisotropic Carbon Nanotube Foams with Tunable Multifunctional Properties**

In this section, we present large scale, ultralight aligned carbon nanotube (CNT) structures which have densities an order of magnitude lower than CNT arrays, have tunable properties and exhibit resiliency after compression. By stacking aligned sheets of carbon nanotubes and then infiltrating with a pyrolytic carbon (PyC), resilient foam-like materials were produced that exhibited complete recovery from 90% compressive strain. With density as low as 3.8 mg/cm<sup>3</sup>, the foam structure is over 500 times less dense than bulk graphite. Microscopy revealed that PyC coated the junctions among CNTs, and also increased CNT surface roughness. These changes in the morphology explain the transition from inelastic behavior to foam-like recovery of the layered CNT sheet structure. Mechanical and thermal properties of the foams were tuned for different applications through variation of PyC deposition duration while dynamic mechanical analysis showed no change in mechanical properties over a large temperature range. Observation of a large and linear electrical resistance change during compression of the anisotropic CNT/carbon (ACNT/C) foams makes strain/pressure sensors a relevant application. The foams have high oil absorption capacities, up to 275 times their own weight, which suggests they may be useful in water treatment and oil spill cleanup. Finally, the ACNT/C foam's high porosity, surface area and stability allow for demonstration of the foams as catalyst support structures.

#### **3.1 Experimental**

##### **3.1.1 MWCNT Synthesis**

Vertically aligned CNT arrays were grown in a tube furnace via a modified version of the chlorine mediated chemical vapor deposition route<sup>56</sup>. The arrays were grown on a quartz substrate at 760 C and 3 Torr with acetylene as the carbon precursor and FeCl<sub>2</sub> (anhydrous 99.5%

VWR) as the catalyst. The arrays were grown for 15 minutes under the flow of acetylene (600 sccm), argon (395 sccm) and chlorine (5 sccm). A detailed procedure of the growth method is explained in previous work<sup>57</sup>.

### 3.1.2 Fabrication of the ACNT/C Foam

Aligned CNT sheets were drawn from arrays and continuously collected around two rotating parallel glass rods to make flat foam pieces. CNT winding continued until the desired sheet thickness was reached. Collecting the sheets around two small, suspended glass rods instead of a large mandrel helped the stack of aligned CNT sheets to be less compacted, resulting in a macro-porous structure. The sheets were then separated from the glass rods using a razor and then placed inside the tube furnace for CVI of PyC. Samples were heated in tube furnace and at 800 °C in vacuum. Acetylene was then allowed to flow at 600 sccm while the pressure was maintained at 30 Torr during the desired deposition time of 60 or 120 minutes. Foam size was only limited by the CVI chamber size.

### 3.1.3 Material Characterization

Scanning electron microscopy (SEM) was conducted on a FEI XHR-Verios 460L field emission SEM (with 1 kV beam voltage and 6.3 pA beam current). All samples were used as prepared without sputtering. Transmission electron microscopy (TEM) images were taken using a JEOL 2000FX TEM operating at 200 kV. To prepare the samples, a small piece of ACNT/C foam was dispersed in ethanol through sonication and a droplet of the dispersion was further deposited on a carbon mesh TEM grid and allowed to dry. The average diameter of pristine and PyC coated nanotubes were calculated by taking 100 measurements from TEM images for each sample using ImageJ software.

### 3.1.4 Mechanical, Electrical and Thermal Measurements

Compression testing was performed on an Instron 5544 equipped with a 100 N load cell and two flat insulating plates. Compressive load was applied either longitudinal or transverse to CNTs alignment direction. Prior to compression testing, a laser cutter (Epilog mini/helix- model 8000) was used to cut the samples into small pieces. Longitudinal samples were cut into 15 x 15 x 15 mm pieces where CNTs were aligned in thickness direction. For transverse samples, foams with dimensions of 15 x 15 x 5 mm were cut where nanotube layers were stacked in the Z direction. All samples were tested for 100 cycles from 0- 90% compressive strain at a rate of 10 mm/min. Four-probe electrical resistance of the foams was also monitored in situ while compressing the samples. Two pieces of copper foil were used as electrodes and silver epoxy glue was applied to adhere the foam to the copper foils. Copper wires were then soldered to the copper foil electrodes. Dynamic mechanical analysis (PerkinElmer DMA 8000) was used to measure storage modulus, loss modulus and damping ratio of the ACNT/C foams at temperature -100 to 300 °C. Foams were compressed with a frequency of 1 Hz while DMA head displacement was 0.025 mm. Room temperature thermal diffusivity was measured in both longitudinal and transverse directions by laser flash measurement technique in a Netzsch laser flash apparatus (LFA447). Longitudinal and transverse samples were cut into 12.7 x 12.7 x 2.5 mm pieces using the laser cutter. Prior to testing, a thin layer of graphite was sprayed on both sides of the samples in order to enhance the absorption of laser energy and emission of infrared (IR) radiation to the detector.

### 3.1.5 ALD of ZnO and Photodeposition Process

ALD of ZnO was performed in a custom built, hot-wall, viscous flow reactor at a temperature of 120 °C, and an operating pressure of 1 Torr. The metallorganic precursor used was diethylzinc (DEZ) (95% Strem Chemicals, Inc.), and the oxidizing agent was high purity water (Sigma Aldrich). Ultra-high purity N<sub>2</sub> (Machine Welders) was used as the carrier gas with a flow rate of approximately 200-300 sccm. The ALD process began with an N<sub>2</sub> purge of 600 seconds followed by a DEZ dose, N<sub>2</sub> purge, H<sub>2</sub>O dose, and N<sub>2</sub> purge. The dosing sequence was repeated for 100 cycles, after which there was a final N<sub>2</sub> purge for 120 seconds. The dose and purge times used in this particular study were DEZ/N<sub>2</sub>/H<sub>2</sub>O/N<sub>2</sub> = 0.4/30/0.2/60 sec. Photodeposition of Ag onto ZnO-coated ACNT/C foams was conducted by first submerging samples in petri dishes containing 30 mL of a stock solution of 1e-3 M AgNO<sub>3</sub> in water. Photoreduction was carried out by exposing the petri dishes to a high-power UVA irradiation source (Intelli-Ray 400, ~ 75 mW/cm<sup>2</sup>) for 30 minutes.

## 3.2 RESULTS AND DISCUSSION

Vertically aligned CNT arrays were grown on quartz substrate using a low pressure, chlorine mediated CVD method. The pristine CNT arrays could be easily drawn horizontally into aligned sheets (Figure 3.1A). Continuous collection of aligned sheets around rotating glass rods allowed for fabrication of CNT structures with any desired thickness (Figure 3.1B). Each wound sheet layer added approximately 30 µm to the thickness of the structure and a 9.5 x 6 x 2.5 cm piece of stacked aligned CNT sheets could be easily drawn from one CNT array (Figure 3.1C). As-drawn aligned CNT structures were not elastic and were permanently deformed after compression. The stack of aligned CNT sheets was then infiltrated with PyC for the desired deposition time of 60 or 120 minutes. These samples are referred to as 60-C and 120-C, respectively. Interestingly, the structural and morphological changes after PyC infiltration made them resilient, exhibiting shape recovery after compression. As a result, ACNT/C foams could be compressed into a pellet and almost fully recover from deformations as large as 90% after removal of the external stress.

This fabrication method is highly unique in that, unlike most other routes, the size of the foams is not limited. Side by side drawing of a number of arrays into aligned sheet allows for fabrication of wider pieces, while placing the rotating glass rods further from each other increases the length of the final piece. Thickness of the foams is controlled by adjusting the duration of drawing process. Density of as-drawn stacked CNT sheets was 1.6 mg/cm<sup>3</sup>, but increased to 3.8 and 9.2 mg/cm<sup>3</sup> after 60 and 120 minutes of PyC infiltration, respectively. This increase in density corresponds to volume fraction rise from 0.0008 to 0.0019 and 0.0046, yielding porosity >99%.

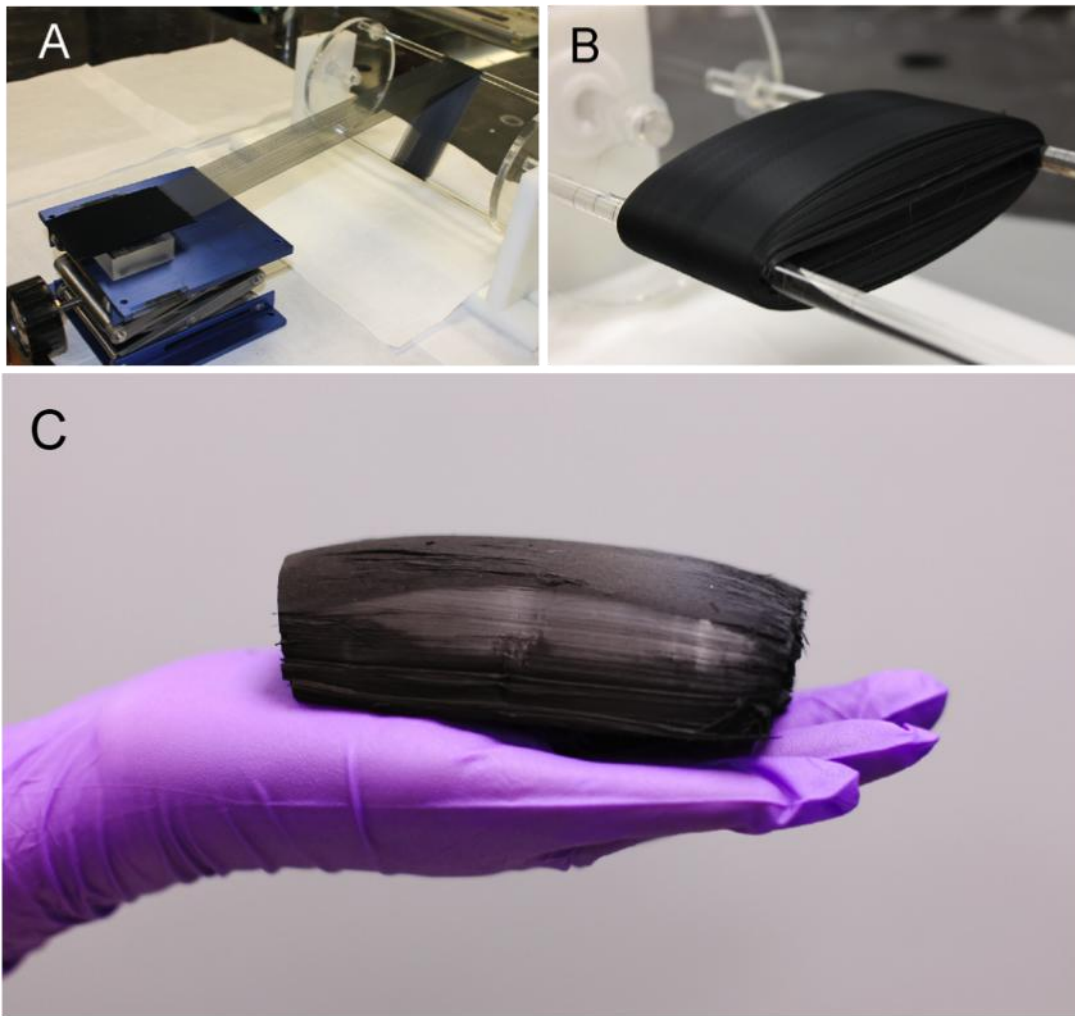


**Figure 3.1** A) Drawing and winding of ACNT sheet. B) A thick, multi-layer ACNT sheet before separation from the glass rods. C) A large ACNT/C foam after infiltration with PyC.

### 3.2.1 Effects of Morphological Changes on Resiliency of ACNT/C Foams

Figure 3.2 shows SEM and TEM images of as-drawn CNTs and ACNT/C foams. The highly porous structure allows for gas infiltration into the CNT network and uniform PyC coating throughout the stacked sheet thickness was observed. The core-shell structure of PyC coated nanotubes is clear in Figure 3.2C & E where the cross section of the coated nanotubes is shown. Measurements from TEM images showed that CNT diameters increased, on average from 31 nm to 78 nm and 148 nm after 60 and 120 minutes PyC coating, respectively. Comparing TEM images of samples 60-C and 120-C revealed that the deposited PyC becomes more disordered as the coating increases in thickness.

Perhaps the most apparent change to the structure after PyC deposition was an increase in CNTs surface roughness. When compressing an as-drawn CNT structure, the van der Waals interactions among smooth walls of nanotubes at points of contact is substantial. Thus, the

structure will remain permanently deformed even after the compressive load is removed. If the surface roughness of the CNTs increases through chemical vapor infiltration (CVI) of PyC, van der Waals interactions among nanotubes decreases, allowing for separation of CNTs inside the foam and recovery of the structure as the compressive load is removed. Another structural change that can contribute to the resiliency of CNT sheets after carbon infiltration is the formation of PyC coated CNT junctions. As shown in SEM images, CNTs in as-drawn sheets are mostly aligned in spinning direction with some points of contact (bundles) between nanotubes in the same or neighboring layers. During CVI post treatment, deposited PyC layers coat these CNT junctions, increasing tube-tube integrity, which resulted in greater structural stability under compression. In other words, *physical cross-links*, in the form of PyC coated junctions, are introduced into the structure through carbon infiltration to freeze-in or reinforce the original sheet state.

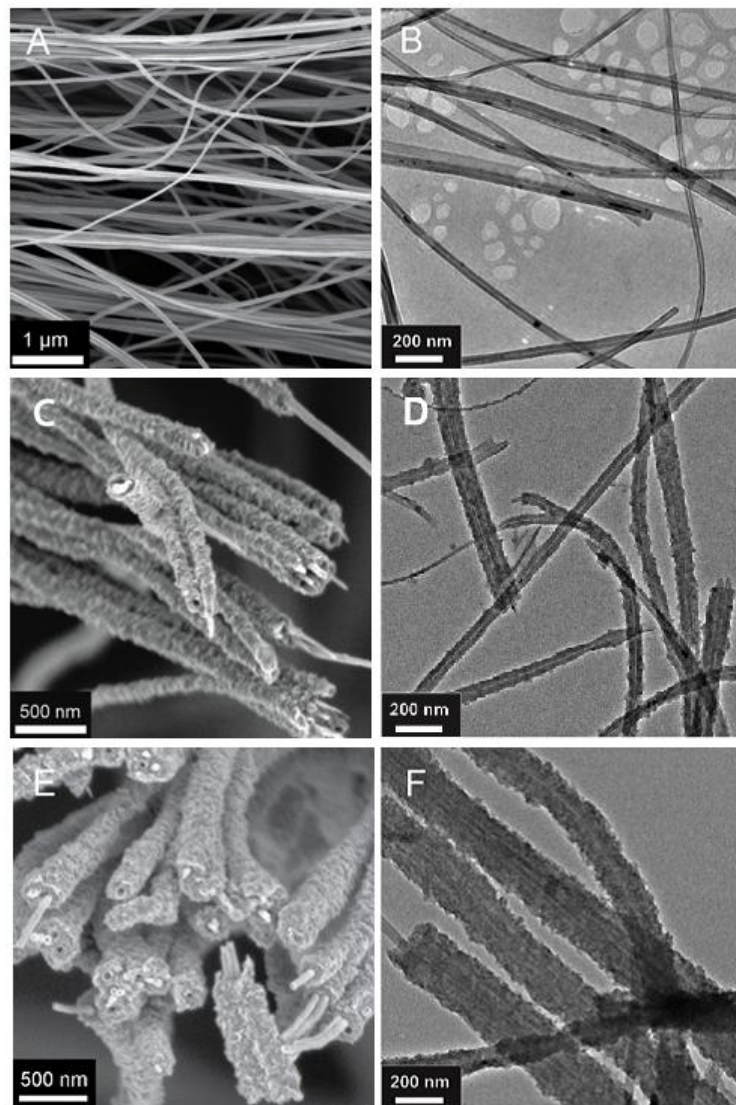


**Figure 3.2** SEM (left) and TEM (right) characterization of samples. A,B) As-spun CNT sheets. C,D) 60-C foam and E,F) 120-C foam

### 3.2.2 Mechanical Behavior

Anisotropic CNT/C foams can be compressed in transverse or longitudinal directions, yielding significantly different mechanical behavior. Mechanical properties of ACNT/C foams could also be tuned for specific applications through varying PyC coating duration. Foams with shorter PyC deposition were compressed more easily than samples with longer PyC infiltration. All samples were tested for 100 cycles at 90% strain. This strain range covers the initial linear region and also shows the plateau and the strain hardening behavior.

Figure 3.3 shows compressive loading-unloading curves for ACNT/C foams with different PyC treatment durations tested in two directions. When compressed in the transverse direction, 60-C foam exhibited a stress of 2.4 kPa at 80% strain. The higher density foam, made with 120 minutes of PyC infiltration, showed more than a 3-fold increase in strength at the same 80% strain. Both foams showed complete shape and structural recovery from the applied stress. During subsequent compression cycles, slow accumulation of permanent compressive deformation resulted in 4.4% and 5.4% residual strain for 60-C and 120-C foams, respectively.

The ACNT/C foams exhibited different mechanical properties when samples were tested parallel to nanotube alignment direction. On the first cycle, compressive strength of both 60-C and 120-C foams at 80% strain was approximately three times greater. For all the samples, further densification of nanotube structure at strain values above 80% resulted in a rapid increase of the modulus.

When the longitudinal structures were compressed, energy absorption and associated energy dissipation (area of the hysteresis loops) were much greater than transversely compressed samples. The energy absorption also increased with increased PyC coating duration. As shown in Figure 3.3A, energy absorption of the foams compressed longitudinally increased and reached about 1150 kJ/m<sup>3</sup> after 120 minutes of PyC infiltration. This is three times greater than the energy absorption of the same foam and more than 14 times greater than that of 60-C foam when they were compressed in the transverse direction. The 120-C foam dissipated 626 kJ/m<sup>3</sup> energy in the initial compression cycle when compressed in longitudinal direction.

Significant hysteresis loops of longitudinal samples during compression testing provided energy loss coefficients (dissipated energy divided by absorbed energy) of 0.47 and 0.54 in the first cycle for 60-C and 120-C foam, respectively. Energy loss coefficients of both samples decreased to ~ 0.40 and was nearly constant after ten cycles.

The observed mechanical behavior (strengthening of the ACNT/C foam by increasing PyC infiltration duration) can be attributed to increased diameter of the nanotubes and also improved stability between CNTs at points of junction. Radial growth of nanotubes through depositing PyC layers increases the critical load required for bending them. While this factor is more important when compressing ACNT/C foams longitudinal to CNT alignment direction, coating nanotube junctions with PyC improves the compression strength in both directions.

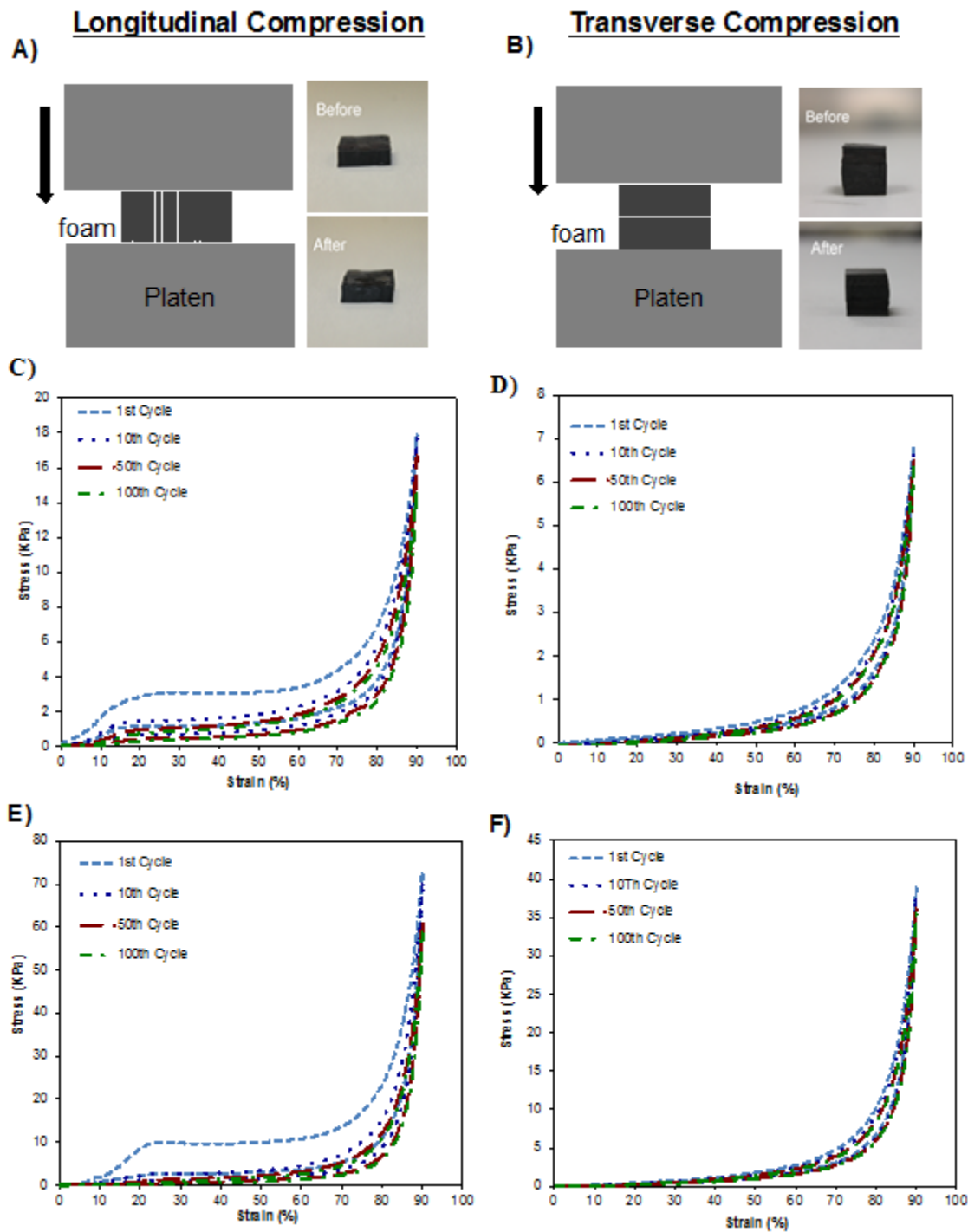


**Figure 3.3** Compression behavior of ACNT/C foams. Schematic illustration of the samples for longitudinal (A) and transverse (B) compression testing with photographs showing foams before and after 100 cycles of compression. Compression loading-unloading curves of 60-C foam (C,D) and 120-C foam (E,F) tested in both directions.

Dynamic mechanical analysis (DMA) was used to further study the elastic properties of ACNT/C foams. Storage modulus, loss modulus and damping ratio of the foams were stable over a large temperature range of -100 to 300 °C. This stability is particularly useful in extreme temperature conditions where traditional polymeric foams are subject to thermal transitions, which dramatically change the mechanical properties. While the DMA instrument capability was limited to 300 °C, previous studies on PyC coated CNTs showed that these structures are stable up to 600 °C before degradation starts.

Storage modulus of the ACNT/C foam increased by one order of magnitude when PyC infiltration duration increased from 60 minutes to 120 minutes. No data was collected for the foams in transverse direction due to limitation of the load cell in the DMA. Figure 3.4B shows the DMA results for longitudinally compressed 120-C foam.

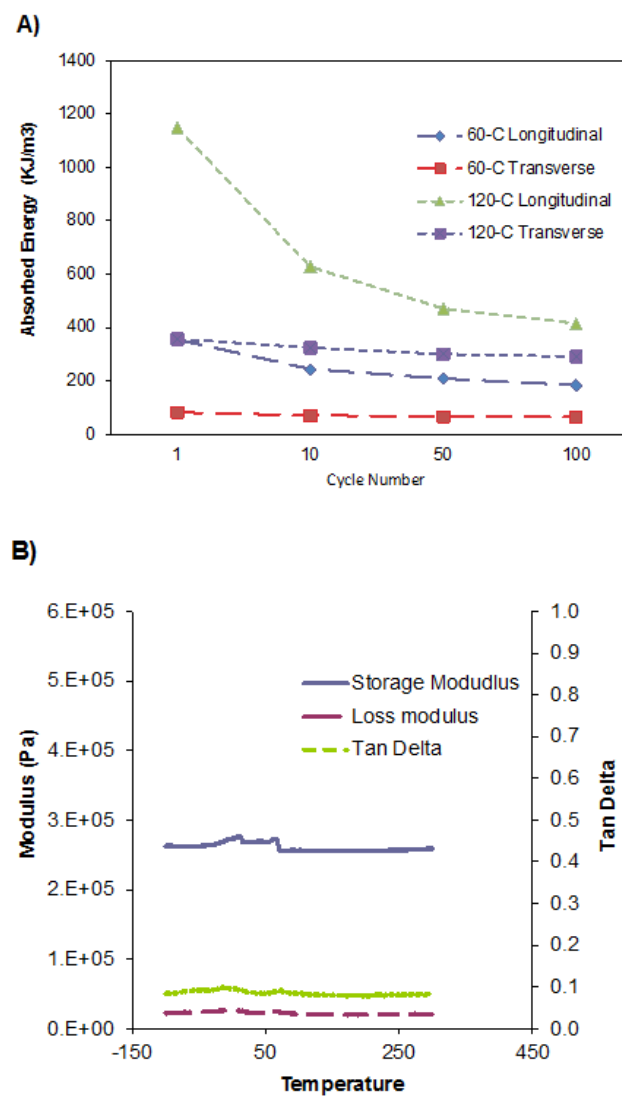


**Figure 3.4** A) Energy absorption of ACNT/C at increasing cycle number. B) DMA data for 120-C foam tested longitudinally.

### 3.2.3 Thermal Properties

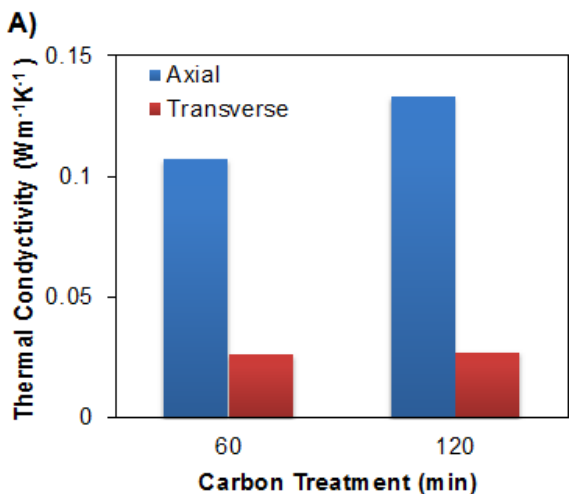
Thermal diffusivity of ACNT/C foams was measured both longitudinal and transverse to nanotube alignment direction. Longitudinal diffusivity of 60-C foam was  $\sim 40 \text{ mm}^2/\text{s}$  when measured at room temperature and pressure. Increasing PyC coating duration to 120 minutes decreased the diffusivity of the foam by nearly half. It is known that phonons and vibrations of the crystal lattice play a dominant role in thermal transport of carbon materials. Interactions between phonons and structural imperfections decrease the phonon mean free path and increase their scattering. Therefore, it is expected that 120-C, having a more disordered structure, would exhibit lower diffusivity. The anisotropic ACNT/C foams exhibited much lower thermal diffusivity in transverse direction:  $\sim 4$  and  $9 \text{ mm}^2/\text{s}$  for 60-C and 120-C samples, respectively.

Thermal conductivity of ACNT/C foams was estimated from thermal diffusivity ( $\alpha$ ), specific heat ( $C_p$ ), and density ( $\rho$ ) and by using the equation  $\lambda = \alpha \times \rho \times C_p$ . Specific heat capacity of CNTs is reported to be very close to that of graphite at temperatures below 300  $^{\circ}\text{K}$ . Assuming that  $C_p$  of PyC coated CNTs is equal to that of pure nanotubes, the specific heat of graphite at the corresponding temperature ( $710 \text{ J kg}^{-1}\text{K}^{-1}$ ) was used for PyC coated CNTs in the calculations. The thermal conductivity of 60-C and 120-C foams in longitudinal direction was calculated as 0.107 and  $0.133 \text{ Wm}^{-1}\text{K}^{-1}$ , respectively.

Due to much lower diffusivity of foams in transverse direction, the estimated thermal conductivities were an order of magnitude lower in that direction and were calculated to be only 0.026 and  $0.027 \text{ Wm}^{-1}\text{K}^{-1}$  for 60-C and 120-C samples, respectively. The super-low thermal conductivities of ACNT/C foams is due to their extremely low densities, as well as their low thermal diffusivities (especially in transverse direction). This thermal conductivity is much lower compared to other CNT macrostructures. In fact, it is close to the lower limit of thermal conductivities of commercial thermal insulation materials ( $0.02\text{-}0.07 \text{ Wm}^{-1}\text{K}^{-1}$ ). The combination of super-low thermal conductivity of ACNT/C foams along with their high temperature stability, could lead to their use as improved insulation for high temperature applications.

It is known that high temperature heat treatments help to remove structural defects and improve crystalline quality in carbon materials. Raman spectroscopy studies on the graphitic structure of similar PyC coated CNT sheets have shown that the average  $I_D / I_G$  of the samples decrease after high temperature heat treatment. To study the effect of annealing on thermal conductivity of ACNT/C foams, samples were heat treated in a high temperature furnace (RED DEVIL vacuum furnace WEBB 124) at  $2150 \text{ }^{\circ}\text{C}$  for five hours in an argon atmosphere. Results showed that after thermal annealing, longitudinal diffusivity of 60-C and 120-C along the nanotube axis increased to 105 and  $60 \text{ mm}^2/\text{s}$ , respectively. This indicates that high temperature heat treatment enhanced the micro-crystallite size and graphitic quality of ACNT/C foams, resulting in fewer scattering centers for phonon propagation and greater thermal diffusivity. Improvement in diffusivity after heat treatment was smaller in transverse direction compared to that of longitudinal direction. This was expected since the low diffusivity of ACNT/C foams in transverse direction was mainly due to limited heat diffusion through the air, which separates the CNT layers. After high temperature annealing the foams became more anisotropic with a 10x difference in the thermal conductivity between longitudinal and transverse directions. Figure 3.5 summarizes the thermal diffusivity of 60-C and 120-C foams in both directions, before and after high temperature heat treatment.

Before High Temperature Annealing



After High Temperature Annealing

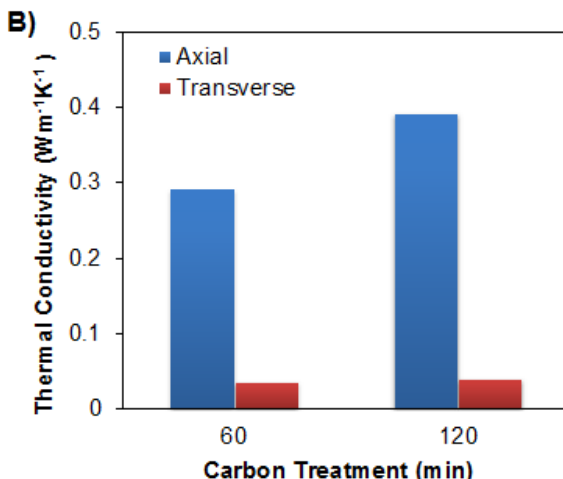


**Figure 3.5** Thermal diffusivity of ACNT/C foams in transverse and longitudinal direction before (A) and after (B) high temperature heat treatment

### 3.2.4 Strain/Pressure Sensors

The dependence of electrical resistance of the foams to applied pressure was investigated *in situ* as the ACNT/C foams were compressed up to ~ 90% in both directions. A schematic of the setup for the *in situ* measurement of electrical resistance during compression is shown in Figure 3.6. The starting resistance of the 60-C foam for transverse configuration with no load was  $10.7\ \Omega$ . Under applied compressive loading, compaction of the adjacent CNT sheet layers caused the normalized electrical resistance ( $R/R_0$ ) to decrease linearly and dramatically, until reaching about 15% of the initial value. Following unloading of the compressive force, complete recovery of the electrical resistance was observed. This behavior was consistent over 100 cycles of loading and unloading (Figure 3.6C). 120-C foam had a lower starting electrical resistance of  $8.2\ \Omega$  and showed a similar resistance change behavior upon cyclic transverse compression.

Longitudinal compression of the foams showed non-linear and less dramatic changes in resistance (Figure 3.6D & F). This is because in longitudinal direction, electrons are mainly travelling along the length of nanotubes and thus, resistance of the foams is less sensitive to developing contact points between CNTs during compression. In comparison, electron transfer in transverse direction almost completely depends on CNT-CNT contact points and resistance is more sensitive to applied compression. Another reason is the distinct behavior of the foams in longitudinal compression compared to transverse. Under transverse loading, nanotubes exhibit uniform compressibility *as an ensemble* and *collective* densification of them leads to linear change in normalized resistance. However, under longitudinal compression, CNTs are bent in a random fashion. Our results showed that the normalized resistance of the 60-C foam changed only 30 %, up to 75% strain. After that, a faster decrease in resistance occurs at higher strain values (> 75%), where CNT foams are compressed enough that more contact points are formed between CNTs. This causes a non-linear change in normalized resistance for samples compressed in the longitudinal direction. The combination of excellent compressive recovery

and high electrical sensitivity to compression, make ACNT/C foams a great candidate for large displacement strain/pressure sensors.

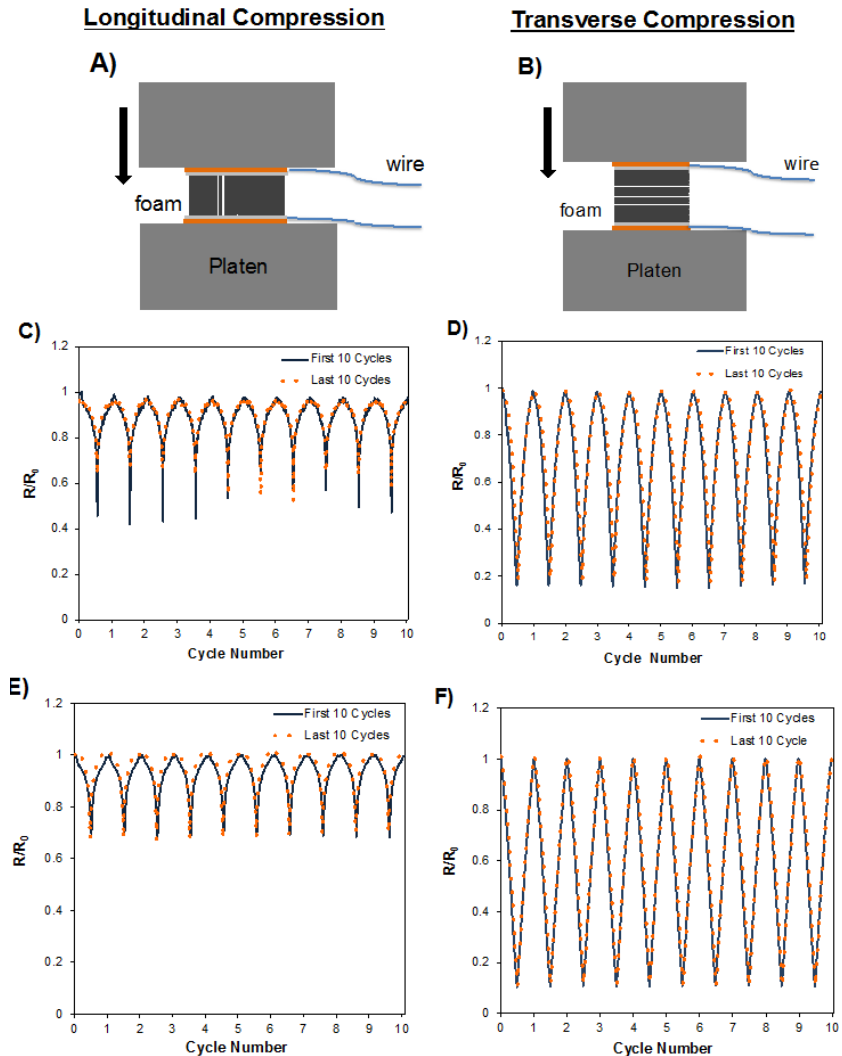


**Figure 3.6** Illustration of sample setup for two-probe electrical resistance measured in-situ for A) longitudinal and B) transverse compression. Changes in electrical resistance for 60-C foam (C,D) and 120-C foam (E,F) tested in two directions.

### 3.2.5 Catalyst Supports

Given their high surface area as well as good chemical and physical stability, ACNT/C foams are excellent catalyst support materials. Zinc oxide, a technologically important wide band gap semiconductor with photocatalytic properties, was conformally deposited onto the ACNT/C foams using atomic layer deposition (ALD). After deposition of the thin oxide layer the ACNT/C foams transitioned from hydrophobic to hydrophilic. To demonstrate the catalytic behavior of the

ZnO-ACNT/C hybrid, photoreduction of Ag was carried out by submerging the samples in a dilute aqueous solution of  $\text{AgNO}_3$  and placing them under a UV lamp. After 30 minutes of UV exposure, an obvious color change from black to silver indicated a dense coating of Ag. This was also verified in SEM images provided in Figure 3.7. This demonstrates the ability to use ACNT/C foams as low density catalyst supports that are dimensionally stable when submerged in liquids.

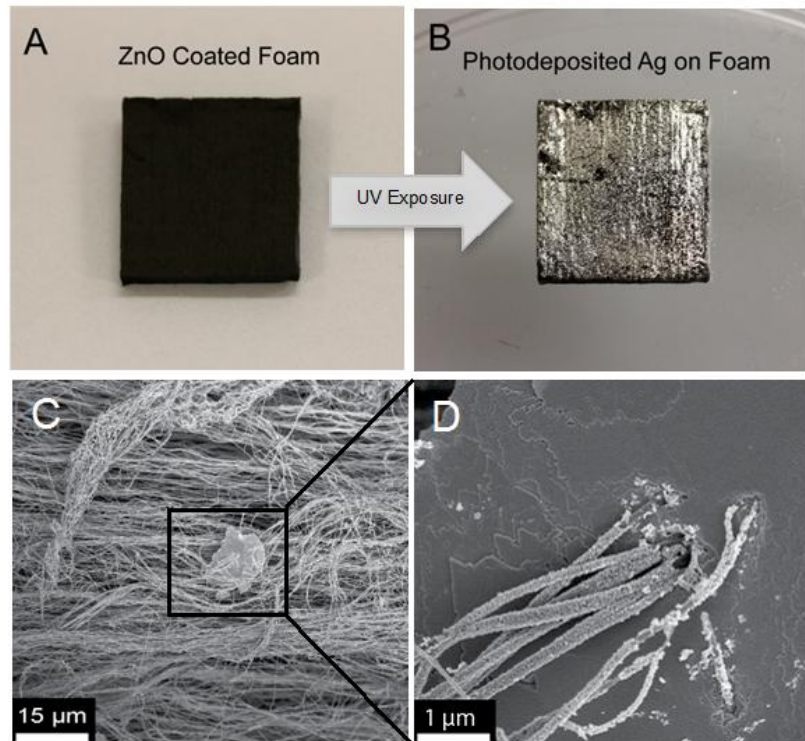


**Figure 3.7** Application of ACNT/C foams as catalyst support materials. A,B) Photograph of ZnO coated foam before and after photodeposition of Ag. C,D) SEM image of photodeposited Ag on ACNT/C foam.

### 3.2.6 Selective Liquid Absorption

ACNT/C foams are highly hydrophobic with contact angle of  $\sim 150^\circ$  but possess high absorption capacities for organic solvents and oils. Absorption capacities,  $Q$  (the ratio of the final weight after full absorption to the initial weight of the foam), for a 60-C foam are presented in Figure 3.8. The foams demonstrated high absorption capacities for various solvents and oils, achieving  $120\text{-}275 \text{ g g}^{-1}$  depending on the liquid density. It should be noted that the foams retained the original shape and size after removal of liquid sorbent by heat.

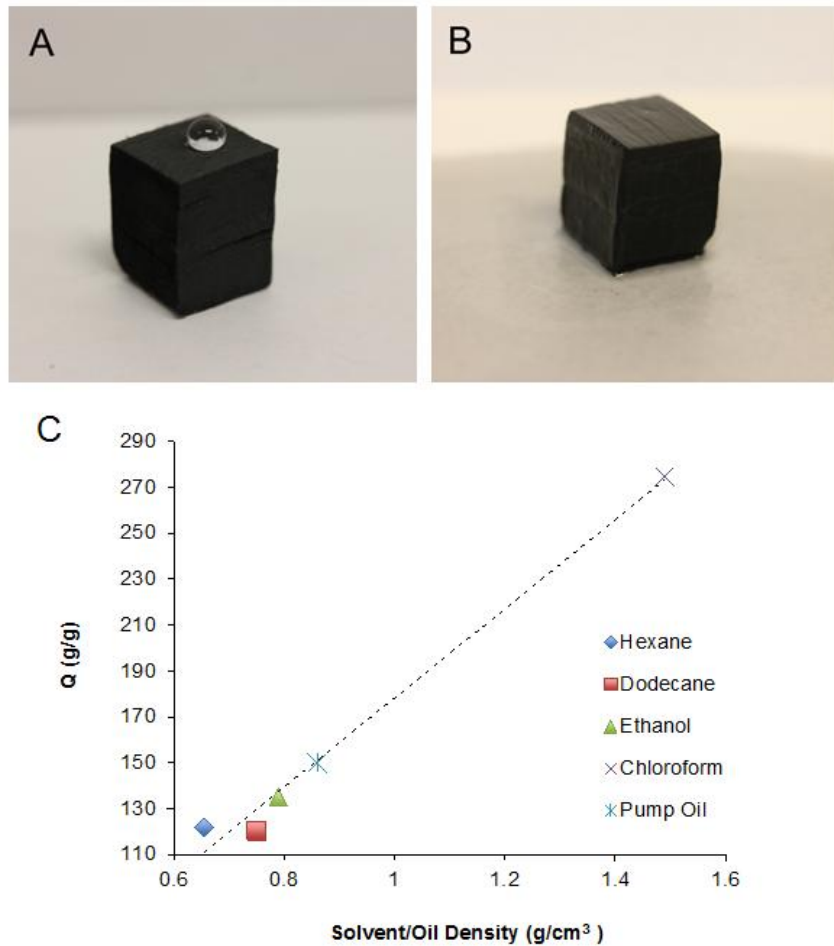


**Figure 3.8** A,B) Photographs showing hydrophobic (A) and oleophilic (B) nature of ACNT/C foams. C) Absorption capacity (Q) of ACNT/C foams measured for a range of organic solvents and oils in terms of their density. The dashed line shows increasing absorption capacity for higher density liquids.

In summary, stacked dry-spun sheets of aligned CNTs were infiltrated with PyC through a CVI method to fabricate anisotropic carbon nanotube foams with ultralow densities. Unlike other routes for fabrication of CNT aerogels, foam and sponges, this processing method allows the fast synthesis of CNT foams with any desired size. Deposition of PyC made the surface of CNTs rough and coated the junctions between nanotubes inside the inter-connected network of the sheet, which led to foam-like recovery of the structure after compression. The ACNT/C foams can be tuned by changing the carbon infiltration time to control thermal transport and mechanical properties. Samples with longer PyC treatment times exhibited greater compressive strength and energy absorption while having lower thermal diffusivity. Super-low thermal conductivities (as low as  $0.026 \text{ W m}^{-1} \text{ K}^{-1}$ ) paired with the known thermal stability of carbon materials, suggests the application of these foams as thermal insulation for high temperature applications. Also,

compressive mechanical properties of ACNT/C foams were unchanged over the large temperature range of -100 to 300 °C as revealed by DMA testing. Electrical resistance of these foams showed stable, linear dependency to applied compressive strain, making these foams acceptable for application as strain/pressure sensors. Oleophilic ACNT/C foams showed great oil absorption capacity, up to 275 times their own weight, making them applicable for water treatment and oil spill cleanup while photoreduction experiments demonstrate the potential of these foams to be used as catalyst support materials.

#### **4. Effect of Carbon Nanotube Length on Thermal, Electrical and Mechanical Properties of CNT/Bismaleimide Composites**

Multi-wall carbon nanotubes (MWCNTs) with lengths of 0.65 to 1.3 mm were used to fabricate aligned and continuous MWCNT/bismaleimide composites. We found that longer CNTs resulted in higher thermal and electrical conductivities of the composites. The tensile strength and Young's modulus, however, exhibited no CNT length dependency. Investigation of the CNT morphology by transmission electron microscopy revealed that the average nanotube diameter and wall number also increased with the CNT length, while the aspect ratio remained nearly unchanged. The structural changes significantly affected the phonon and electron transport in the composite structure, but the interplay of increased CNT length and diameter led to no appreciable change in the mechanical properties of the composites.

Aligned arrays of MWCNTs were grown on quartz substrates by a one-step chemical vapor deposition (CVD) method using  $\text{FeCl}_2$  as the catalyst. The MWCNTs with 0.65, 0.8, 0.9, 1.1 and 1.3 mm in length were grown for 8, 10, 11, 14 and 16 min, respectively. The MWCNT arrays were self-oriented and highly drawable, i.e., CNT sheets could be pulled out from the arrays and converted into continuous films. The matrix system, liquid BMI resin with a molecular weight of 5000, was obtained from Designer Molecules Inc. The BMI solution was prepared by diluting the resin in toluene (99.8% anhydrous, Sigma-Aldrich). The MWCNT/BMI composite prepgs were fabricated using the “spray winding” approach described in previous sections. We used a sprayer to deliver  $2.5 \text{ g L}^{-1}$  BMI/toluene solution in a layer-by-layer fashion as the CNT sheet was wound onto a rotating spool. The composite prepgs were degassed in a vacuum oven at 90 °C for 2 h to eliminate the entrapped air and to remove the residual toluene. The prepgs were then compressed between two glass blocks and cured at 180 °C for 2 h. The resultant composite films had a thickness of 10-15  $\mu\text{m}$  and a typical CNT weight fraction of approximately 35%.

##### **4.1 Thermal Conductivities**

The thermal transport properties of the CNT/BMI composites strongly depend on the CNT length, as shown in Figure 4.1 and Table 4.1. The 0.65 mm CNTs with tubular diameter of 37 nm produced composites with the lowest thermal conductivity of 33 W/m·K. The composites composed of 1.1 mm CNTs with tubular diameter around 59 nm showed the highest thermal conductivity of 70 W/m·K, demonstrating a 112% improvement over the composites containing 0.65 mm-long CNTs. Further increase in CNT length and diameter did not improve the thermal conductivity, reaching a saturation level. Pristine aligned CNT film without polymer was

reported to have a thermal conductivity of 70 W/m·K. It is worth noting that when assembling CNTs into large-scale composites, it is difficult to make full use of the excellent thermal conductivity of individual CNTs (3000 W/m·K). Weak tube-tube coupling, dangling tube ends, misalignment and high density of defects all contribute to quenching of phonon modes and thus decrease the thermal conductivity of the composites.

Heat transport in CNT/polymer composites is carried out by phonons of various wavelengths. The near-linear increasing trend for composites produced with 0.65-1.1 mm CNTs could be explained by noting that the CNT lengths are much longer than the mean free path of phonons in the sample. The effect of short wavelength phonons probably reaches a stable level while the long wavelength phonons continue to contribute to the heat transport process. As a result, a longer and thicker CNT would amount to a more efficient heat conduction path, which also allows the transport of phonons with longer wavelengths. In addition, larger-diameter MWCNTs are more likely to form a rigid and compact structure and thus reduce the thermal contact resistance at the intertube and tube-polymer interfaces. For CNT/BMI composites that are produced with millimeter-long nanotubes, we believe that it is the direct conduction path along the CNTs and the large specific surface area other than interfacial thermal resistance that significantly affect the heat conduction in the composites, similar to graphene-based composites. Otherwise the CNT/BMI composites should exhibit a much lower thermal conductivity. Figure 4.2 is a model that describes the thermal conducting mechanism proposed for our CNT/BMI composites, in which thermal conduction along the tubes is dominant over conduction across the interfaces. In comparison, for short nanotube-reinforced composites, the phonon mobility is restricted at the interface as a result of the thermally insulating nature of polymer. In such case, the overall thermal conductivity is mechanistically limited by the high CNT/polymer interfacial thermal resistance.

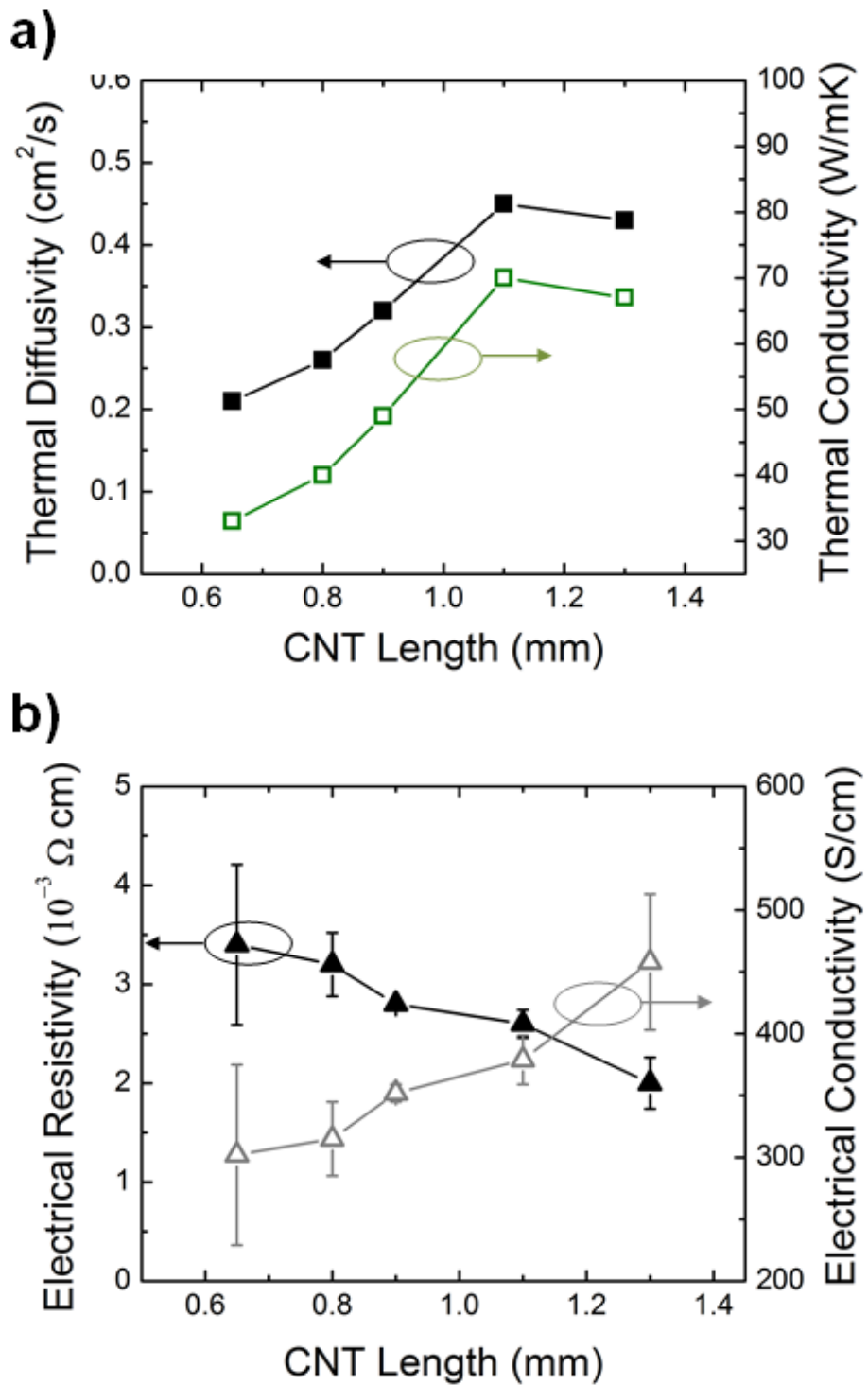


**Figure 4.1** Effect of CNT length on (a) thermal diffusivity and corresponding thermal conductivity, and (b) electrical resistance and conductivity of CNT/BMI composites.

**Table 4.1** Thermal and electrical properties of CNT/BMI composites produced using CNTs with different lengths.

CNT length in composite (mm)	Tensile strength (MPa)	Young's modulus (GPa)	Thermal conductivity (W/m·K)	Electrical conductivity (S/cm)
0.65	395.0±89.0	27.9±8.3	33	302
0.8	383.1±90.1	35.0±8.3	40	315
0.9	249.2±48.2	17.4±6.5	49	352
1.1	332.2±96.9	25.6±5.6	70	379
1.3	544.9±110.0	38.4±7.9	67	458

1 – Conducting along the nanotube  
2 – Conducting across the interfaces

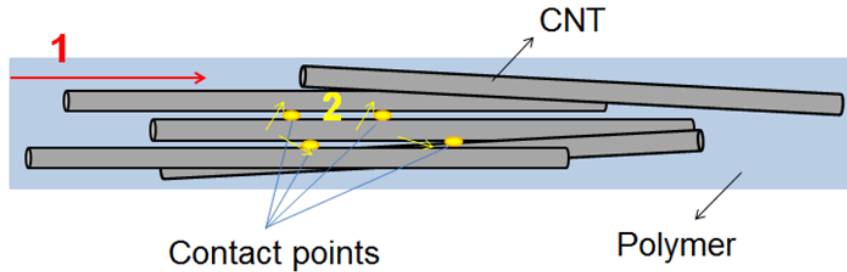


**Figure 4.2** Schematic presentation of heat conduction mechanism in CNT/BMI composites containing high volume fraction of long and aligned nanotubes.

The prerequisite for investigating CNT length effect on thermal conductivities of composites is a near-ideal structure of the composites. Factors including CNT length, volume fraction, alignment and contact area all contribute to the efficiency of phonon transport in the composites. In this work, the CNT/BMI composites containing 35 wt% aligned nanotubes exhibit a remarkably high thermal conductivity (~30-70 W/m·K), much higher than previously reported short CNT composites fabricated by dispersion method (0.6-4 W/m·K). This is because that CNT composites fabricated by the “spray winding” approach are composed of long and well aligned nanotubes, which enables the utilization of intrinsic thermal properties of CNTs. Additionally, a high volume fraction of CNTs are well dispersed and densely packed in the polymer matrix due to the layer-by-layer spraying process, which ensures a strong tube-tube coupling and allows a large volume of graphene shells participating in the phonon transport. Moreover, as demonstrated by the TEM image and Raman spectrum, the CNTs have a high degree of graphitization and few defects. On such basis, with lengths exceeding several hundred

microns, the CNTs exhibit expected exceptional thermal conductivity along the CNT length orientation.

#### 4.2 Electrical Conductivities

Similarly as observed in the thermal conductivity, the electrical conductivity of CNT/BMI composites depended greatly on the CNT length and diameter (shown in Figure 4.1 and Table 4.1). This trend is also evident for electrical conductivity: the increase in CNT length and diameter led to increased electrical conductivity. For example, the electrical resistance decreased monotonically from  $3.4 \times 10^{-3} \Omega \cdot \text{cm}$  at the CNT length of 0.65 mm to  $2.0 \times 10^{-3} \Omega \cdot \text{cm}$  at the CNT length of 1.3 mm. The calculated electrical conductivity increased from 302 S/cm to 458 S/cm accordingly. The CNT structures may affect the composite electrical conductivity in two ways: i) longer and thicker CNTs ensure a more effective electron conduction path along the individual nanotubes, similar to the thermal conduction mechanism; ii) CNTs with larger diameters favor more compact structures so that separation (tunneling distance) between CNTs decreases.

#### 4.3 Mechanical properties of CNT/BMI composites

The mechanical properties of the CNT/BMI composites are summarized in Table 4.1. Unlike the thermal and electrical conductivities, the tensile strength and Young's modulus of the CNT/BMI composites do not present an apparent relationship with the CNT length. The composites fabricated using 1.3 mm-long CNTs demonstrated the highest tensile strength ( $544.9 \pm 110.0$  MPa) and Young's modulus ( $38.4 \pm 7.9$  GPa) among all the samples. However, those composites produced with CNTs at the lower range of the length spectrum (0.6-1.1 mm) did not exhibit any trend in the mechanical property improvement. In addition, no noticeable difference in alignment can be observed based on the SEM images in Figure 4.3.

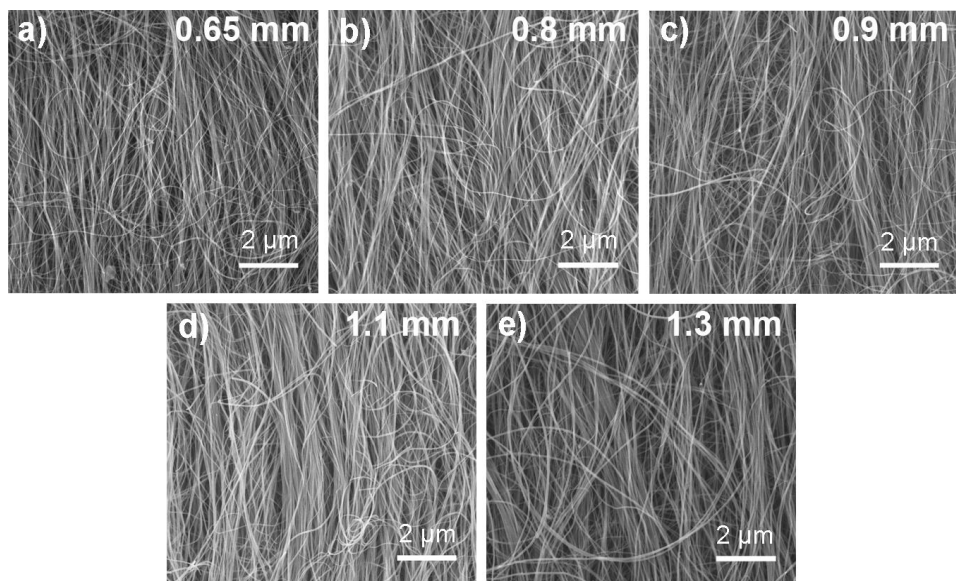


**Figure 4.3** SEM images of CNT structures in the CNT/BMI composites fabricated using CNTs with different lengths.

In order to maximize composite strength and stiffness, long tubes (large aspect ratio) are desired, because the mechanical properties of composites scale directly with the total interfacial surface area, which is determined by the CNT aspect ratio. Note that the elastic properties of composites are particularly sensitive to the tube diameter, since larger-diameter nanotubes with greater wall numbers may exhibit lower effective modulus due to wall slippage. In this work, although the CNT length increased with the growth time, the aspect ratio of the CNTs with different lengths remained unchanged due to the enlarged tube diameter. Therefore, the almost unchanged mechanical properties of CNT/BMI composites seem to be a consequence of the unchanged CNT aspect ratio, which is in agreement with previous studies. Moreover, the tensile strength of the composites is statistically determined by the size and form of defects that define how much load the first-to-fail defect region bonds carry in uniform axial loading. Hence, the tensile strength of the CNT/BMI composites is also complicated by such factors as CNT quality and structural uniformity.

In this work, the CNT/BMI composites show a tensile strength of 240-550 MPa and Young's modulus of 17-38 GPa. The composite structure has met the requirement of long CNT length, high degree of alignment, high CNT volume fraction and individualized dispersion of nanotubes in the matrix. As a result, the composites obtained reasonably good properties compared to composites produced by conventional dispersion method. However, the tensile strength and Young's modulus are much lower than those of the composites reported in previous work. This is because the nanotubes used here are many-walled ( $> 20$ ) and the outer diameter is very large ( $> 20$  nm), which may render larger amount of defects (imperfection in crystallization) and wall slippage in the CNT structures. To further improve the mechanical properties of the composite materials, small diameter and few-walled CNTs should be employed.

## **5. Ultrastrong, Stiff and Multifunctional Carbon Nanotube Composites**

We developed a stretch-winding process (see Figure 5.1) to make CNT composites with unprecedented multifunctionalities, including record high strength (3.8 GPa), Young's modulus (293 GPa), electrical conductivity ( $1230 \text{ S}\cdot\text{cm}^{-1}$ ) and thermal conductivity ( $40 \text{ W m}^{-1}\cdot\text{K}^{-1}$ ). These superior properties are derived from the long length, high volume fraction, good alignment and reduced waviness of the CNTs, which were produced by a novel processing approach that can be easily scaled up for industrial production.

The key component of our strategy for fabricating high strength CNT composites is to straighten the wavy CNTs before embedding them into a polymer matrix, as illustrated in Figure 5.1a. The unidirectional CNT sheets used in this study were converted from superaligned CNT arrays that were synthesized by a chemical vapor deposition (CVD) method. The CNTs were multi-walled (MWNTs) with outer diameter of 7-9 nm and 4-6 walls (as shown in the Supplementary online material). The density of the nanotube was calculated as  $1.46 \text{ g cm}^{-3}$  based on the average CNT inner and outer diameters. The strong van der Waals inter-tube interaction enables the drawing of continuous and uniform CNT sheets, in which the CNTs are largely aligned in the drawing direction. However, individual nanotubes are wavy microscopically.

In a stretch-winding process as shown in Figure 5.1b, the CNT sheet travels horizontally and passes through a tensioning system. As the CNT sheet passes around a pair of stationary rods, the

increased tension stretches the CNT sheets. The contact angle between the CNT sheet and the stretching rods was controlled at 150-165°. The CNT sheet was stretched according to a stretch ratio  $((L_S - L_0)/L_0$ , where  $L_S$  and  $L_0$  are the length of the CNT sheet before and after stretching, respectively. The stretched CNT sheet was then wound onto a rotating cylindrical polytetrafluoroethylene (PTFE) spool.

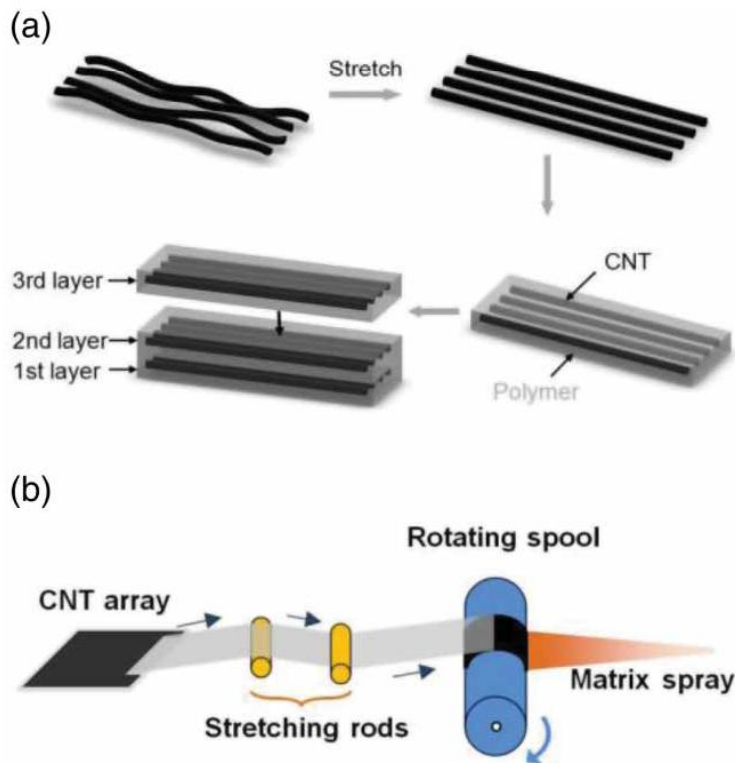


**Figure 5.1** (a) Schematic illustration of the concept of straightening CNTs before embedding them in polymer matrix in a layer-by-layer fashion. (b) Schematic illustration of the experimental setup for the stretch-winding process.

For real-world applications such as aerospace structures, a stronger and lighter material allows greater degree of flexibility and capacity. As shown in Figure 5.2a, our strongest CNT composites is at least 15% stronger than the current best engineering composites, and far higher than those for CNT composites reported previously. In addition, our composites have a lower density of  $1.4 \text{ g}\cdot\text{cm}^{-3}$ . Consequently, the specific strength of our CNT composites is at least 30% higher than that for the best engineering composites, as shown in Figure 5.2b.

The stretch-wound CNT composites have shown an ultrahigh tensile strength of up to 3.8 GPa and a specific strength of up to  $2.7 \times 10^7 \text{ cm}$ , which represents a significant breakthrough in

engineering materials. The average strength and stiffness of four CNT composite samples are 3.5 GPa and 266 GPa, respectively (see the Supplementary online material). Figure 5.3a shows the tensile engineering stress-strain curves of pristine CNT sheet without matrix and CNT composite sheets stretched to various stretch ratios. As shown, the pristine CNT sheet has strength of 300 MPa and Young's modulus of 21 GPa. The unstretched composites exhibited strength of 2.0 GPa and Young's modulus of 130 GPa. The stretching raised the strength and Young's modulus to as high as 3.8 GPa and 293 GPa, respectively, at the stretch ratio of 12% (Figures 5.3b and 5.3c). The density of the stretch-wound composites was  $1.4 \text{ g}\cdot\text{cm}^{-3}$ , as compared to  $1.6 \text{ g}\cdot\text{cm}^{-3}$  for CFRP with a typical 60% fiber by volume. The lower density renders the stretch-wound composites higher specific strength and specific stiffness. The toughness of the stretch-wound composites, calculated as the area under the stress-strain curves, reached  $22 \pm 5 \text{ J}\cdot\text{g}^{-1}$ , which is comparable to toughened CFRP and higher than that of the recently reported high-strength CNT/BMI composites ( $<15 \text{ J}\cdot\text{g}^{-1}$ ). The higher toughness ensures safer composite structures with higher damage tolerance.

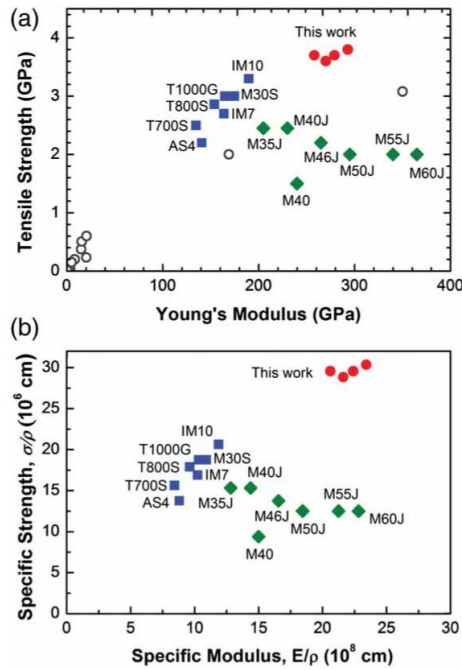


**Figure 5.2** (a) Comparison of the tensile strength and Young's Modulus of currently available engineering carbon fiber reinforced polymer composites (CFRP) as well as CNT composites reported previously. Note that all data are from composite samples. The blue filled squares are from existing high-strength CFRP and the green filled diamonds are from those of currently existing high-modulus CFRP. The unfilled circles are best CNT composites reported previously. (b) Comparison of the specific tensile strength and specific modulus of the stretch-wound composites with the best engineering CFRP. The data were calculated based on a density of  $1.6 \text{ g cm}^{-3}$  for CFRP (60 vol.%) and  $1.4 \text{ g cm}^{-3}$  for the stretch-wound composites (46 vol.%).

The room temperature thermal properties of CNT/BMI composites with different stretch ratio are presented in Figure 5.3d. The in-plane thermal diffusivities of the composite sheet along the CNT alignment direction,  $\alpha$ , were measured using a scanning laser heating analyzer (Ulvac-Riko, Inc., Laser PIT). The thermal conductivities of the composites,  $\lambda$ , were calculated using  $\lambda = \alpha \rho C$ , where  $\rho$  is the density and  $C$  is the specific heat of the composite. The in-plane thermal diffusivity of the 12%-stretched composites averaged  $27 \text{ mm}^2 \cdot \text{s}^{-1}$  (see the Supplementary online material), which is 3 times as high as the value of unstretched composites. For the nanocomposites with 50 vol.% CNTs, the calculated  $\lambda$  value is  $40 \text{ W} \cdot \text{m}^{-1} \cdot \text{K}^{-1}$ , which is higher than that of unidirectional Polyacrylonitrile based CFRP ( $4.5 \text{ W} \cdot \text{m}^{-1} \cdot \text{K}^{-1}$ ) and other reported high volume fraction CNT composites ( $0.4\text{--}1.3 \text{ W} \cdot \text{m}^{-1} \cdot \text{K}^{-1}$ ). These results indicate that stretching improves the alignment and straightness of CNTs and promotes a more efficient transfer of phonons along the CNT length direction of the composites.

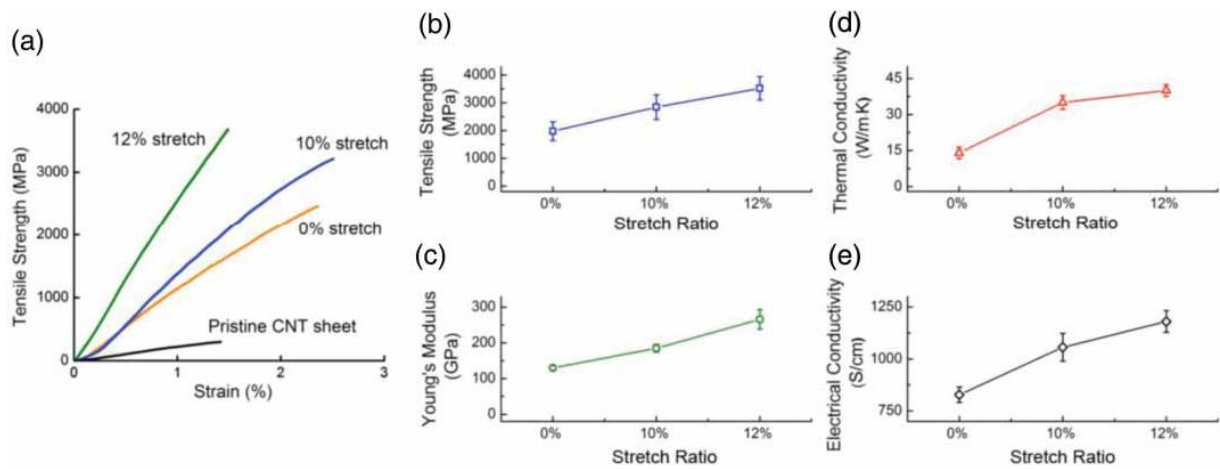


**Figure 5.3** (a) Typical stress-strain curves of pristine CNT sheet, unstretched and stretched composites, demonstrating a significant improvement of the mechanical properties through aligning and straightening of CNTs. Effect of stretching on (b) tensile strength and (c) Young's modulus, (d) thermal conductivity, and (e) electrical conductivity of the composites.

Composites with straightened CNTs also revealed excellent electrical conductivities because the inter-tube contacts for electron transfer were facilitated by the improved CNT alignment and reduced waviness. The pristine CNT sheets, which were condensed with ethanol, had a highly porous structure and thus a relatively low conductivity of  $570 \text{ S} \cdot \text{cm}^{-1}$ . The unstretched composites showed an electrical conductivity of  $820 \text{ S} \cdot \text{cm}^{-1}$ , in which the capillary force of dilute BMI solution drew and held the CNTs close to each other. As shown in Figure 5.3e, the electrical conductivity of the composites increases monotonically with increasing stretch ratio. Composite sheets that are stretched for 12% have the highest level of CNT alignment and straightness among all of the samples and thus the highest conductivity of  $1230 \text{ S} \cdot \text{cm}^{-1}$ , which is a 116% increase over the pristine CNT sheets.

## **6. Micro-combing Makes High Performance Carbon Nanotube Composite Films**

In order to maximize the carbon nanotube (CNT) buckypaper properties, it is critical to improve their alignment and reduce their waviness. Here a novel approach, micro-combing, is developed to fabricate aligned CNT films with a uniform structure. High level of nanotube alignment and straightness was achieved using sharp surgical blades with micro-sized features at the blade edges to comb single layers of CNT sheet. These micro-combs also reduced structural defects within the film and enhanced the nanotube packing density. Following the micro-combing approach, as-produced CNT films demonstrated a tensile strength of up to 3.2 GPa, Young's modulus of up to 172 GPa, and electrical conductivity of up to  $1.8 \times 10^5$  S/m, which are much superior to previously reported CNT films or buckypapers. More importantly, this novel technique requires less rigorous process control and can construct CNT films with reproducible properties.

### **6.1 Experimental**

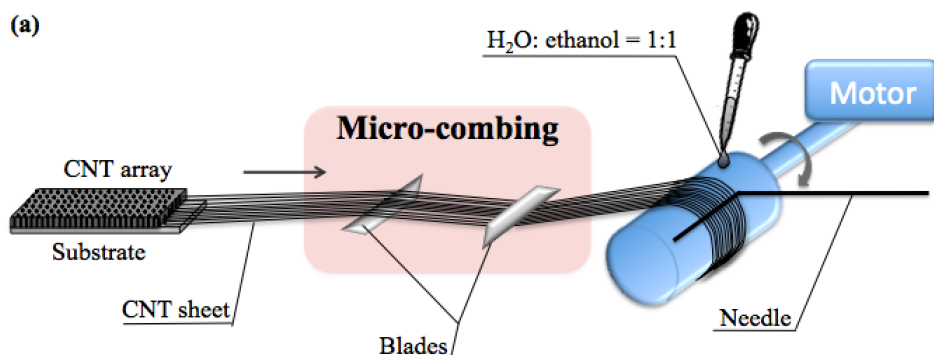
#### **6.1.1 Materials**

The drawable CNT arrays used in the experiment were synthesized using a CVD method. The CNT arrays were approximately 200  $\mu\text{m}$  in height, with individual nanotubes having 2~5 walls and 5~7 nm in diameters.

#### **6.1.2 Micro-combing process**

The key component of the process, micro-combing of individual layer of CNT sheets, is accomplished by using two oppositely positioned surgical blades. As shown by the schematics in Figure 6.1, when a layer of CNT sheet is drawn out from the CNT array, it passes two surgical blades, then wound to a rotating mandrel with a diameter of 3 cm at a speed of 20 r/min. The contact angle between the CNT sheet and the blade was controlled at  $80^\circ\sim85^\circ$ . A metal needle with a diameter of 0.65 mm bent into  $90^\circ$  was placed on the mandrel at 1 o'clock position, coating the densifying solution on the CNT sheet layer by layer during the winding process, as shown in Figure 6.1b. The densifying solution consists of deionized water and ethanol with a mixing ratio of 1:1 by volume.

Two hundred revolutions produced a film with a thickness of about 3  $\mu\text{m}$ . The CNT film was then peeled off from the mandrel and hot-pressed at 80°C for 2 hrs under a pressure of 10 MPa. Under high pressure, the film was condensed to about 2  $\mu\text{m}$ . Since the coating solution was  $\text{H}_2\text{O}$  and ethanol, they evaporated during the process, leaving a pure dry CNT film with aligned long CNTs.



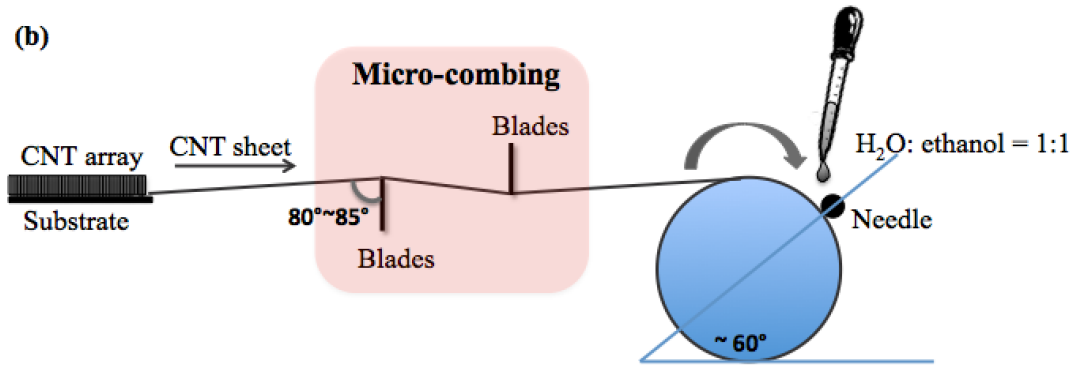


**Figure 6.1** Micro-combing process: (a) schematic overview; (b) schematic side view

## 6.2 Results and discussion

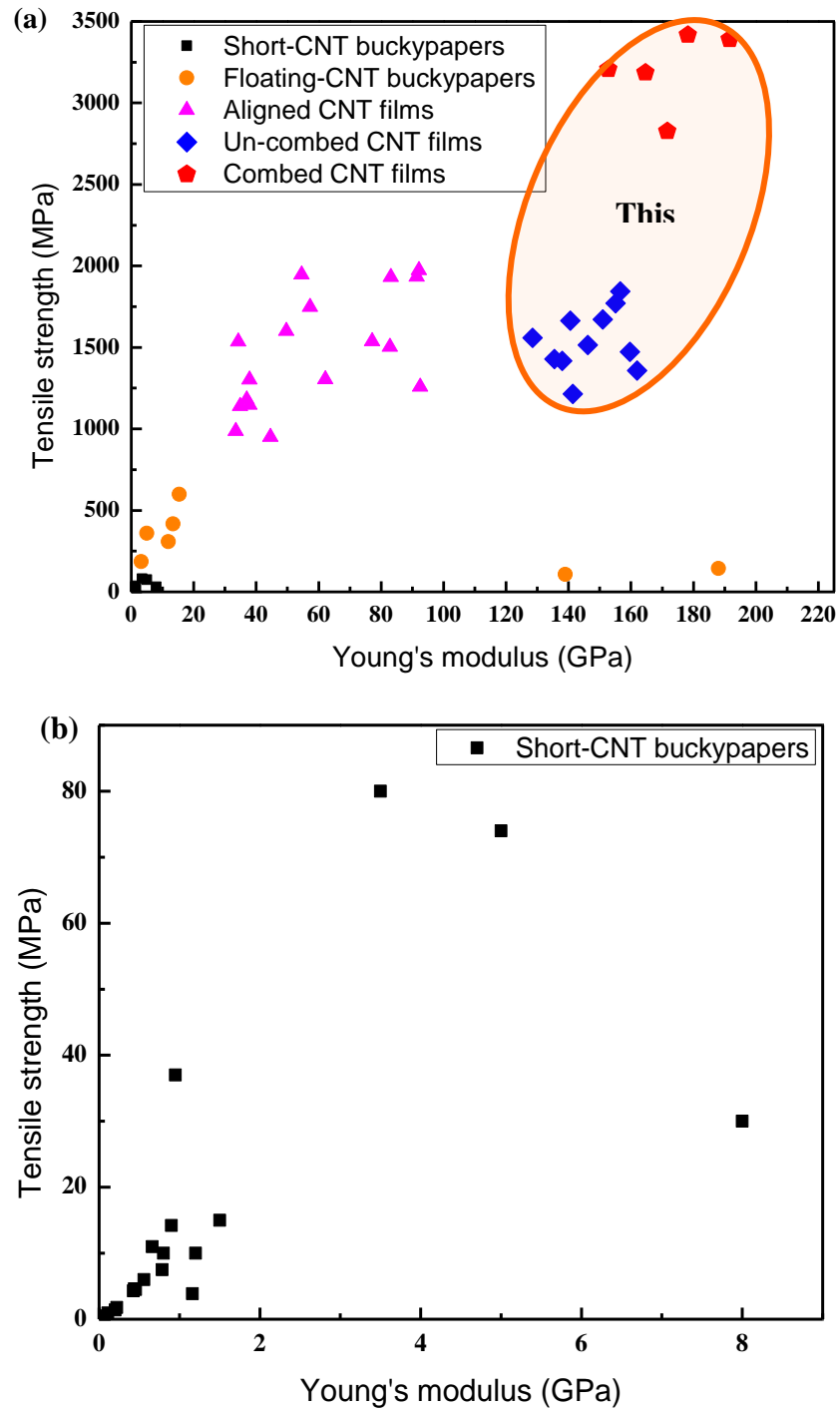
### 6.2.1 Mechanical properties

Table 6.1 and Figure 6.2 compare the mechanical properties of the dry CNT films produced by micro-combing with previously reported data. The CNT buckypapers made of short CNTs are named as short-CNT buckypapers. The buckypapers produced by floating catalyst chemical vapor deposition (FCCVD) method are called floating-CNT buckypapers, and the CNT films made by winding 2D CNT sheet from the drawable arrays are called aligned CNT films. The tensile strength of the as-produced un-combed dry CNT films of 1.56 GPa agrees well with the previously reported data for aligned CNT films (1.0 ~ 2.0 GPa). By micro-combing, the tensile strength of the CNT film was improved by 105% from 1.56 GPa to 3.21 GPa, which surpasses the mechanical properties of CNT films or buckypapers reported earlier. Also, the Young's modulus has a ~14% increase to 171.78 GPa compared to the un-combed films. The density of the un-combed dry films is 0.84 g/cm<sup>3</sup>, whereas the density of the combed dry films is 1.04 g/cm<sup>3</sup>. Thus, the specific tensile strength of the combed dry CNT films is calculated to be 3.08 GPa g/cm<sup>3</sup>. The higher density of the combed dry CNT films indicates enhanced nanotube packing resulted from micro-combing. In comparison, the reported density of the aligned CNT films is typically 0.9 g/cm<sup>3</sup><sup>30</sup>, which is lower than our combed films. With a higher packing density, the aligned CNTs have a stronger inter-tube interaction, which in turn results in a more effective load transfer in the structure.

Figure 6.3 displays typical tensile stress-strain curves for the un-combed and combed dry CNT films. The slopes of the combed films show an apparent change compared to the un-combed ones. The Young's modulus is significantly improved by the micro-combing. This is a direct evidence of the reduction of the CNT waviness and the improvement in the CNT alignment. In addition, the combed CNT films exhibit a higher tensile strain than that of the un-combed films, suggesting a reduction of structural defects induced by micro-combing. The micro-combing is simple, effective, and does not require a narrow window of controlled parameters, which greatly promotes the reproducibility and repeatability of the film properties.

**Table 6.1** Mechanical property comparison for buckypapers and dry CNT films

Type	Material	Treatment	Young's modulus (GPa)	Tensile strength (MPa)	Ref.
Short-CNT buckypapers	SWCNT		1.2	10	15
	SWCNT	HNO <sub>3</sub>	0.8 5	10 74	16
	SWCNT	SOCl <sub>2</sub>	0.66 0.95	11 37	17
	SWCNT	Irradiation	1.5 3.5	6 ~ 15 80	18
	MWCNT		0.4 ~ 0.8	4.3 ~ 7.5	19
	SWCNT		0.9	14.2	20
	SWCNT	Oleum + heat	8	30	21
	MWCNT	Chemicals	0.08 ~ 1.16	0.42 ~ 3.88	22
Floating-CNT buckypapers	SWCNT	Stretch	3.2 ± 0.5	186 ± 19	
		Stretch+Press Once	11.9 ± 0.6	307 ± 28	
		Stretch+Press Twice	13.4 ± 0.5	416 ± 25	26
			15.4 ± 1.0	598 ± 36	
	SWCNT	Purification	188 139	144 107	27
Aligned CNT films	SWCNT		5	360	28
	Few-walled CNT		33.4 ~ 92.5	950 ~ 1973	30
	Few-walled CNT	Un-combed Combed	151.16 ± 17.65 171.78 ± 13.02	1561.05 ± 187.93 3205.71 ± 211.65	This work



**Figure 6.2** Mechanical properties of CNT films: (a) comparison of combed CNT films with previously reported buckypapers and other aligned CNT films; (b) enlargement of the data area for buckypapers produced by short CNT dispersion.

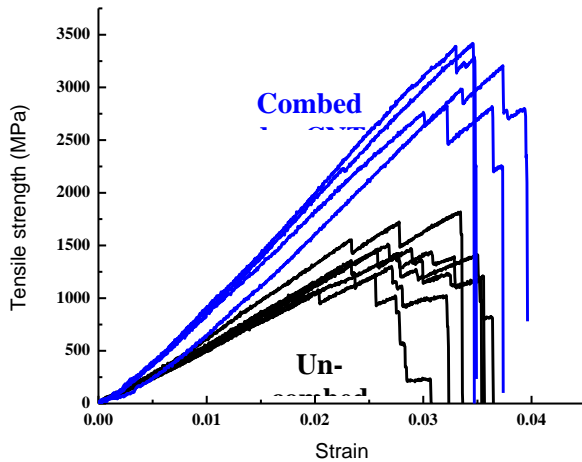


**Figure 6.3** Typical tensile strength curves of the un-combed and combed dry CNT films

## 6.2.2 Electrical properties

Table 6.2 compares the electrical conductivity of the combed CNT films and other CNT buckypapers and films. Figure 6.4 shows the effect of micro-combing on the electrical conductivity of the as-produced dry CNT films. The un-combed CNT films exhibit a high electrical conductivity of  $1.0 \times 10^5$  S/m, which is among the highest reported values. After micro-combing, the electrical conductivity is further improved by 80% to  $1.8 \times 10^5$  S/m. This substantial increase in electrical conductivity is also a direct result from better intertube contact to facilitate electron transfer due to the improved CNT straightness, enhanced CNT alignment, and higher nanotube packing density.

**Table 6.2** Electrical conductivity values of the CNT films produced in our work and the data from the literature

Type	Material	Treatment	Electrical conductivity (S/m)	Ref.
Short-CNT buckypapers	SWCNT	$\text{HNO}_3$	$3 \times 10^4$ $1.2 \times 10^4$	16
	SWCNT	$\text{SOCl}_2$	$7 \times 10^4$ $3.5 \times 10^5$	17
	MWCNT		$0.83 \times 10^4 \sim 1.0 \times 10^4$	19
	SWCNT	Oleum	$1.3 \times 10^5$	21
		Oleum + heat	$9 \times 10^4$	
	MWCNT	Chemicals	$6.53 \times 10^2 \sim 18.18 \times 10^2$	22
	MWCNT	Oriented	$1.5 \times 10^4$ $2 \times 10^4$	24
Floating-CNT buckypapers	SWCNT		$2 \times 10^5$	28
Aligned CNT films	MWCNT		$4 \times 10^4$	29
	Few-walled CNT		$3.5 \times 10^4$	30
	Few-walled CNT	Un-combed Combed	$1.0 \times 10^5 \pm 1156$ $1.8 \times 10^5 \pm 21173$	This work

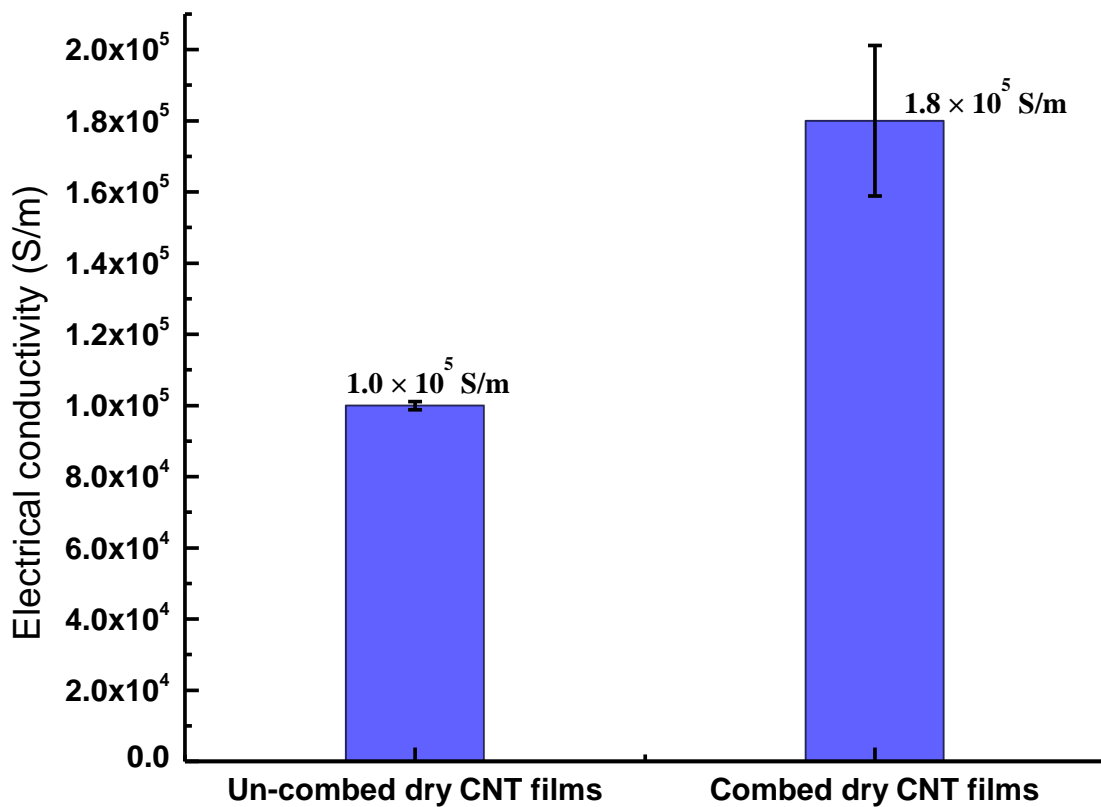


**Figure 6.4** Electrical conductivity of the un-combed and combed dry CNT films

### 6.2.3 Effect of micro-combing on the CNT structure

Combing, which has been used for centuries in the textile industry, is a process to disentangle and straighten staple fibers in order to achieve higher level of fiber alignment in the web<sup>33</sup>. In this work, sharp surgical blades with micro-scale features at the blade edge, were used to disentangle and straighten the wavy CNTs in the as-drawn CNT sheet. The micrometer-sized features of a surgical blade are shown in Figure 6.5.

Figure 6.6 shows both the optical photos and SEM images of the dry CNT sheets before and after micro-combing, and before and after solution treatment, respectively. After the micro-combing process, it is evident that the CNT sheets become shiny due to their smoothed surfaces (Figures 6.6a & b). As shown in the SEM images (Figures 6.6b, c, e, f), the micro-combing process reduced the waviness of CNTs and enhanced the structural uniformity. This is also demonstrated by the TEM images of a single layer of CNT sheet before and after micro-combing, as shown in Figure 6.7. After solution treatment (Figures 6.6e & f), the nanotubes formed larger bundles and the sheets became denser. This was caused by the shrinking and densification effect of the ethanol in the coating solution.

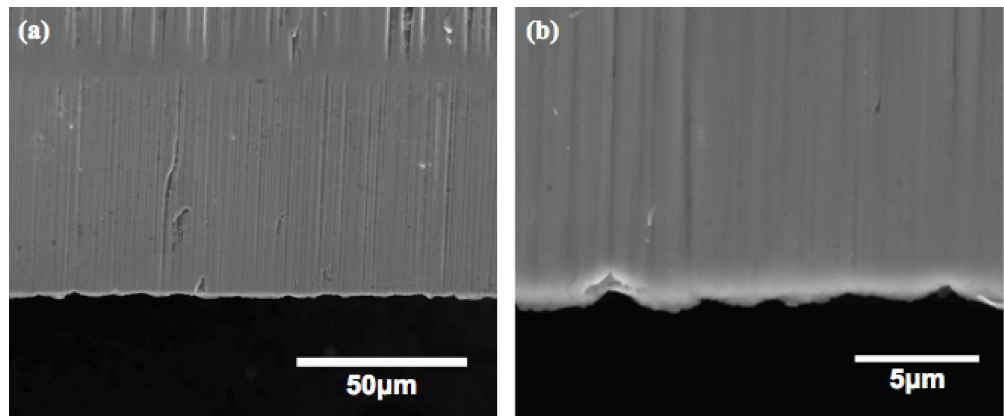


**Figure 6.5** Morphologies of the edge of the micro-combing blade.

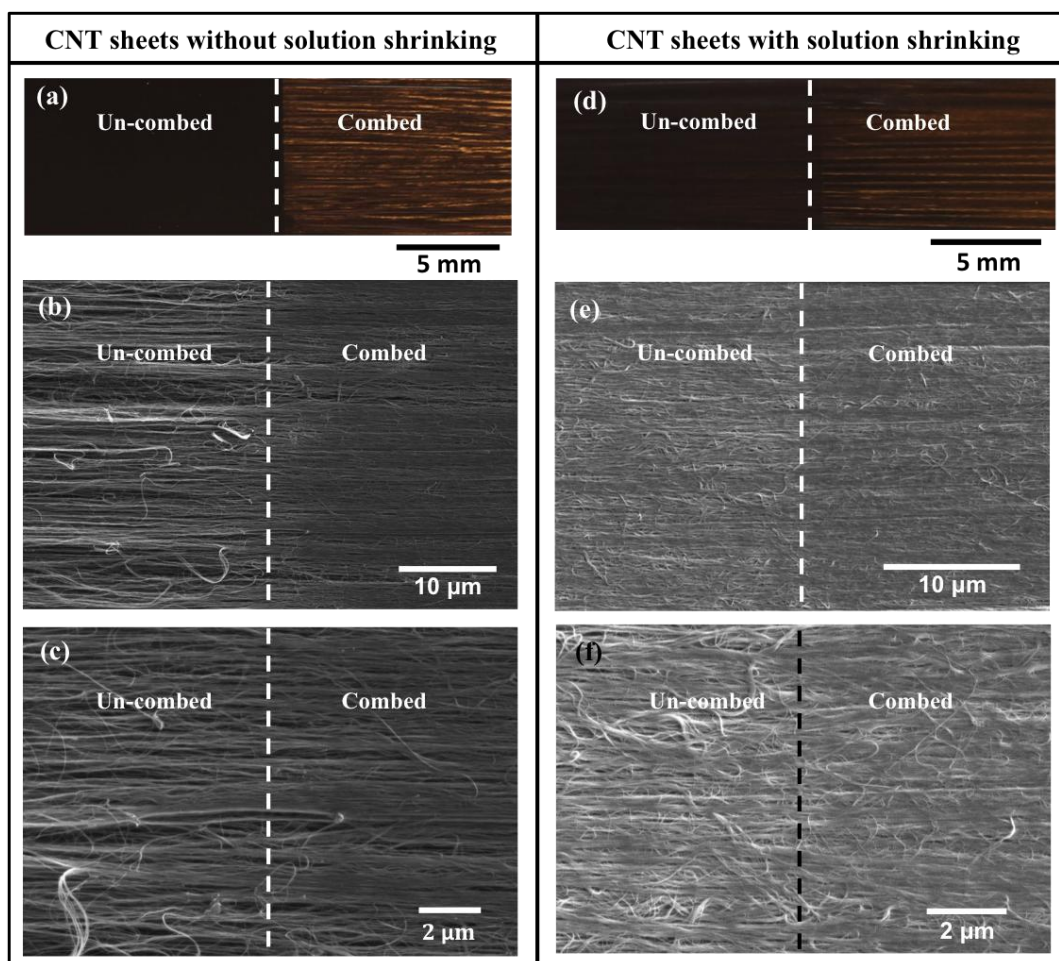


**Figure 6.6** Optical photos (a, d) and SEM images (b, c, e, f) showing the differences between the un-combed and combed dry CNT sheets.

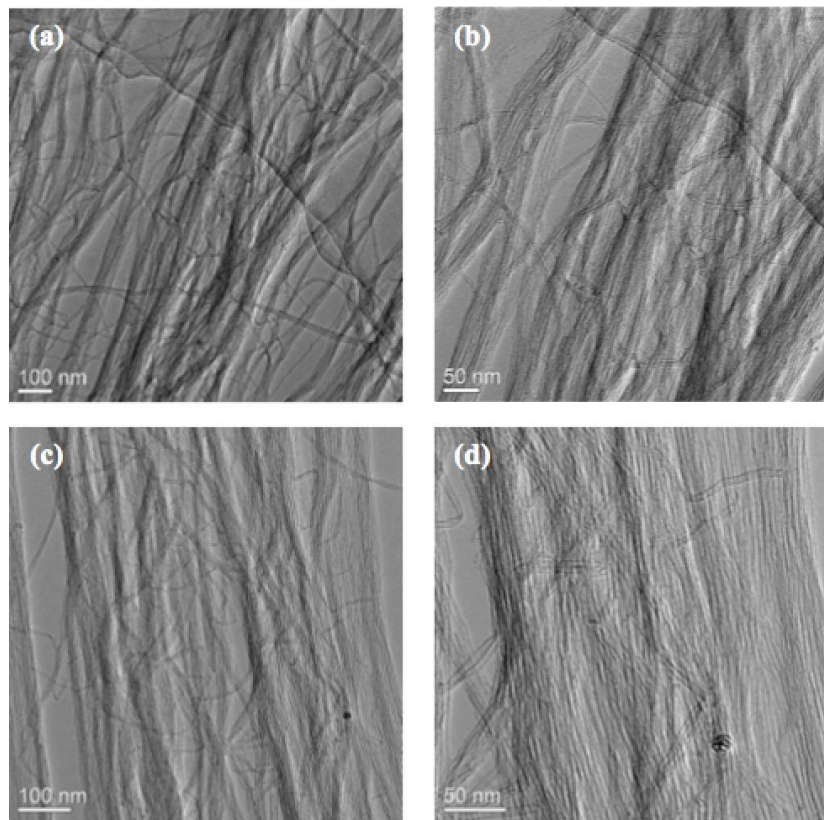


**Figure 6.7** TEM images of one single layer of CNT sheet before (a, b) and after micro-combing (c, d).

### Publications Resulting From this Grant

1. X. Wang, Q. Jiang, W.Z. Xu, W. Cai, Y. Inoue, and Y.T. Zhu, “Effect of Carbon Nanotube Length on Thermal, Electrical and Mechanical Properties of CNT/Bismaleimide Composites,” *Carbon* 53, 145-152 (2013).
2. X. Wang, Z.Z. Yong, Q.W. Li, P.D. Bradford, Q. Jiang, W. Liu, D.S. Tucker, H. Wang, F.G. Yuan, and Y.T. Zhu, “Ultrastrong, Stiff and Multifunctional Carbon Nanotube Composites,” *Mater. Res. Lett.* 1 (1), 19-25 (2013). DOI:10.1080/21663831.2012.686586
3. Q. Jiang, X. Wang, Y.T. Zhu, and Y.P. Qiu, “Mechanical, Electrical and Thermal Properties of Aligned Carbon Nanotube/Polyimide Composites,” *Composites B*, 56, 408-412 (2013).
4. V. Thiagarajan, X. Wang, P.D. Bradford, Y.T. Zhu, and F.G. Yuan, “Stabilizing Carbon Nanotube Yarn Using Chemical Vapor Infiltration,” *Composite Sci. Tech.* 90, 82-87 (2014).
5. Z. Zhou, X. Wang, S. Faraji, P.D. Bradford, Q.W. Li, and Y.T. Zhu, “Mechanical and Electrical Properties of Aligned Carbon Nanotube/Carbon Matrix Composites, “ *Carbon*,

75, 307-313 (2014).

6. P. Gu, M. Dao, and Y.T. Zhu, "Strengthening at Nanoscaled Coherent Twin Boundary in f.c.c. Metals," *Phil. Mag.*, 94(11), 1249-1262 (2014).
7. S. Faraji, K. Stano, C. Rost, J.P. Maria, Y.T. Zhu and P.D. Bradford, "Structural Annealing of Carbon Coated Aligned Multi-Walled Carbon Nanotube Sheets," *Carbon*, 79, 113-122 (2014).
8. J.T. Di, X. Wang, Y.J. Xing, Q.W. Li, and Y.T. Zhu, "Dry-Processable Carbon Nanotubes for Functional Devices and Composites," *Small*, 10, 4606-4625 (2014).
9. P. Gu, Y.T. Zhu and S.N. Mathaudhu, "A Model for  $\langle c+a \rangle$  Dislocation Transmission Cross Nano-Spaced Parallel Basal Stacking Faults in a HCP Alloy," *Phil. Mag. Lett.* 95, 58-66 (2015).
10. L.W. Zhang, X. Wang, W.Z. Xu, Y.Y. Zhang, Q.W. Li, P.D. Bradford, and Y.T. Zhu, "Strong and Conductive Dry CNT Films by Micro-Combing," *Small*, in press.
11. X. Wang, H. West, T.W. Chou, and Y.T. Zhu, "In-Situ Strain Sensing of Glass Fiber Reinforced Composites under Static and Dynamic Cyclic Bending using Embedded Flexible Twisted CNT fibers," *Nanotechnology*, to be submitted.
12. S. Faraji, K. Stano, O. Yildiz, A. Li, Y.T. Zhu, and P.D. Bradford, "Resilient Anisotropic Carbon Nanotube Foams with Tunable Multifunctional Properties," *Nanoscale*, submitted
13. C.Y. Gao, Y. Lu, Y.T. Zhu and Y.L. Ke, "A New Micromechanical Model of CNT-Metal Nanocomposites with Random Clustered distribution of CNTs," *J. Mater. Sci.* submitted.
14. L.W. Zhang, X. Wang, R. Li, Q.W. Li, P.D. Bradford, and Y.T. Zhu, "Micro-combing Makes High Performance Carbon Nanotube Composite Films," *Comp. Sci. Tech.* to be submitted.

### Book Chapters:

1. X. Wang, P.D. Bradford, Q.W. Li, and Y.T. Zhu, "Aligned Carbon Nanotube Composite Prepregs," in *Nanotube Superfiber Materials: Changing Engineering Design*, edited by M.J. Schulz, V.N. Shanov, and Z.Z. Yin, Elsevier, 2014, pp. 649-670.
2. X. Wang, J.T. Di, Q.W. Li, P.D. Bradford, and Y.T. Zhu, "High Performance Composite Based on Dry-Processable Multi-walled Carbon nanotubes," in *Hollow Composites*

### Patent Disclosures

1. Y.T. Zhu, X. Wang, C.D. Page, L.W. Zhang, "Low Twist CNT Yarns for High Performance Textile and Composites," NCSU disclosure # 13087.
2. L.W. Zhang, X. Wang, Y.Y. Zhang, Q.W. Li, Y.T. Zhu, "Processing CNT Films and Composites using Micro-combing to Straighten CNTs," NCSU Disclosure # 15169.

**Awards of the PI and Co-PI during this project period:**

PI: Yuntian Zhu

- Fellow, American Association for the Advancement of Science (AAAS) (2012)
- TMS SMD Distinguished Scientist/Engineer Award, 2012
- Albert Sauveur Achievement Award, ASM International, 2014
- Alcoa Foundation Distinguished Engineering Research Award, NC State University, 2014
- Highly Cited Researchers 2014, among 147 in Materials Science, Thomson Reuters (ISI)
- Leadership Award, TMS, 2015

Co-PI: Philip Bradford

- Outstanding Teacher Award, NC State University 2014
- NC State AIF Best Paper Award, 2013
- Young Faculty Research Award, Sigma Xi Research Society, 2013

1.

**1. Report Type**

Final Report

**Primary Contact E-mail**

**Contact email if there is a problem with the report.**

ytzhu@ncsu.edu

**Primary Contact Phone Number**

**Contact phone number if there is a problem with the report**

919-513-0559

**Organization / Institution name**

North Carolina State University

**Grant/Contract Title**

**The full title of the funded effort.**

Bonding Unidirectional Carbon Nanotube with Carbon for High Performance, Low Density Composites

**Grant/Contract Number**

**AFOSR assigned control number. It must begin with "FA9550" or "F49620" or "FA2386".**

FA9550-12-1-0088

**Principal Investigator Name**

**The full name of the principal investigator on the grant or contract.**

Yuntian Zhu

**Program Manager**

**The AFOSR Program Manager currently assigned to the award**

Joycelyn Harrison

**Reporting Period Start Date**

03/15/2012

**Reporting Period End Date**

03/14/2015

**Abstract**

Producing unidirectional carbon nanotube (CNT) composites with a structural morphology identical to aerospace grade carbon fiber composites is a challenging task that until this work, no research groups had accomplished. This research team demonstrated the ability to produce high volume fraction CNT composites with a high level of alignment, low level of CNT waviness and uniform distribution of polymer surrounding the CNTs. This was accomplished through a process called spray winding. In this process polymer solution was sprayed onto aligned CNT sheets as they were taken up onto a mandrel. In addition, a micro-combing technique was developed where a razor blade was used to further aligned and straighten CNTs within the CNT sheets during winding. The ability to integrate a matrix material at the molecular level among long, highly aligned CNTs allowed for record breaking specific strengths, higher than their carbon fiber composite counterparts. In addition to CNT-polymer matrix composites, the team produced CNT-carbon matrix composites that have a morphology that resembles carbon fiber-carbon composites utilized in the aerospace industry, with a nanostructured architecture of aligned CNTs.

**Distribution Statement**

**This is block 12 on the SF298 form.**

Distribution A - Approved for Public Release

## Explanation for Distribution Statement

If this is not approved for public release, please provide a short explanation. E.g., contains proprietary information.

## SF298 Form

Please attach your **SF298** form. A blank SF298 can be found [here](#). Please do not password protect or secure the PDF. The maximum file size for an SF298 is 50MB.

[AFD-070820-035 2 Zhu.pdf](#)

**Upload the Report Document. File must be a PDF. Please do not password protect or secure the PDF . The maximum file size for the Report Document is 50MB.**

[AFOSR 2015 Final Report.pdf](#)

**Upload a Report Document, if any. The maximum file size for the Report Document is 50MB.**

### Archival Publications (published) during reporting period:

1. X. Wang, Q. Jiang, W.Z. Xu, W. Cai, Y. Inoue, and Y.T. Zhu, "Effect of Carbon Nanotube Length on Thermal, Electrical and Mechanical Properties of CNT/Bismaleimide Composites," *Carbon* 53, 145-152 (2013).
2. X. Wang, Z.Z. Yong, Q.W. Li, P.D. Bradford, Q. Jiang, W. Liu, D.S. Tucker, H. Wang, F.G. Yuan, and Y.T. Zhu, "Ultrastrong, Stiff and Multifunctional Carbon Nanotube Composites," *Mater. Res. Lett.* 1 (1), 19-25 (2013). DOI:10.1080/21663831.2012.686586
3. Q. Jiang, X. Wang, Y.T. Zhu, and Y.P. Qiu, "Mechanical, Electrical and Thermal Properties of Aligned Carbon Nanotube/Polyimide Composites," *Composites B*, 56, 408-412 (2013).
4. V. Thiagarajan, X. Wang, P.D. Bradford, Y.T. Zhu, and F.G. Yuan, "Stabilizing Carbon Nanotube Yarn Using Chemical Vapor Infiltration," *Composite Sci. Tech.* 90, 82-87 (2014).
5. Z. Zhou, X. Wang, S. Faraji, P.D. Bradford, Q.W. Li, and Y.T. Zhu, "Mechanical and Electrical Properties of Aligned Carbon Nanotube/Carbon Matrix Composites," *Carbon*, 75, 307-313 (2014).
6. P. Gu, M. Dao, and Y.T. Zhu, "Strengthening at Nanoscaled Coherent Twin Boundary in f.c.c. Metals," *Phil. Mag.*, 94(11), 1249-1262 (2014).
7. S. Faraji, K. Stano, C. Rost, J.P. Maria, Y.T. Zhu and P.D. Bradford, "Structural Annealing of Carbon Coated Aligned Multi-Walled Carbon Nanotube Sheets," *Carbon*, 79, 113-122 (2014).
8. J.T. Di, X. Wang, Y.J. Xing, Q.W. Li, and Y.T. Zhu, "Dry-Processable Carbon Nanotubes for Functional Devices and Composites," *Small*, 10, 4606-4625 (2014).
9. P. Gu, Y.T. Zhu and S.N. Mathaudhu, "A Model for Dislocation Transmission Cross Nano-Spaced Parallel Basal Stacking Faults in a HCP Alloy," *Phil. Mag. Lett.* 95, 58-66 (2015).
10. L.W. Zhang, X. Wang, W.Z. Xu, Y.Y. Zhang, Q.W. Li, P.D. Bradford, and Y.T. Zhu, "Strong and Conductive Dry CNT Films by Micro-Combing," *Small*, in press.
11. X. Wang, H. West, T.W. Chou, and Y.T. Zhu, "In-Situ Strain Sensing of Glass Fiber Reinforced Composites under Static and Dynamic Cyclic Bending using Embedded Flexible Twisted CNT fibers," *Nanotechnology*, to be submitted.
12. S. Faraji, K. Stano, O. Yildiz, A. Li, Y.T. Zhu, and P.D. Bradford, "Resilient Anisotropic Carbon Nanotube Foams with Tunable Multifunctional Properties," *Nanoscale*. submitted
13. C.Y. Gao, Y. Lu, Y.T. Zhu and Y.L. Ke, "A New Micromechanical Model of CNT-Metal Nanocomposites with Random Clustered distribution of CNTs," *J. Mater. Sci.* submitted.

14. L.W. Zhang, X. Wang, R. Li, Q.W. LI, P.D. Bradford, and Y.T. Zhu, "Micro-combing Makes High Performance Carbon Nanotube Composite Films, " Comp. Sci. Tech. to be submitted.

**Changes in research objectives (if any):**

**Change in AFOSR Program Manager, if any:**

**Extensions granted or milestones slipped, if any:**

**AFOSR LRIR Number**

**LRIR Title**

**Reporting Period**

**Laboratory Task Manager**

**Program Officer**

**Research Objectives**

**Technical Summary**

**Funding Summary by Cost Category (by FY, \$K)**

	Starting FY	FY+1	FY+2
Salary			
Equipment/Facilities			
Supplies			
Total			

**Report Document**

**Report Document - Text Analysis**

**Report Document - Text Analysis**

**Appendix Documents**

**2. Thank You**

**E-mail user**

Jun 13, 2015 22:30:52 Success: Email Sent to: ytzhu@ncsu.edu